

Asteroseismology for “à la carte” stellar age-dating and weighing

Age and mass of the CoRoT exoplanet host HD 52265

Y. Lebreton^{1,2} and M.J. Goupil³

¹ Observatoire de Paris, GEPI, CNRS UMR 8111, F-92195 Meudon, France

² Institut de Physique de Rennes, Université de Rennes 1, CNRS UMR 6251, F-35042 Rennes, France
e-mail: yveline.lebreton@obsppm.fr

³ Observatoire de Paris, LESIA, CNRS UMR 8109, F-92195 Meudon, France

Received , 2012; accepted , 2012

ABSTRACT

Context. In the context of space missions CoRoT, Kepler, Gaia, TESS, and PLATO, precise and accurate stellar ages, masses and radii are of paramount importance. For instance, they are crucial to constrain scenarios of planetary formation and evolution.

Aims. We aim at quantifying how detailed stellar modelling can improve the accuracy and precision on age and mass of individual stars. To that end, we adopt a multifaceted approach where we examine carefully how the number of observational constraints as well as the uncertainties on observations and on model input physics impact the results of age-dating and weighing.

Methods. We modelled in details the exoplanet host-star HD 52265, a main sequence, solar-like oscillator that CoRoT observed for four months. We considered different sets of observational constraints (Hertzsprung-Russell data, metallicity, various sets of seismic constraints). For each case, we determined the age, mass, and properties of HD 52265 inferred from stellar models, and we quantified the impact of the models input physics and free parameters. We also compared models ages with ages derived by empirical methods or Hertzsprung-Russell diagram inversion.

Results. For our case study HD 52265, our seismic analysis provides an age $A = 2.10 - 2.54$ Gyr, a mass $M = 1.14 - 1.32 M_{\odot}$, and a radius $R = 1.30 - 1.34 R_{\odot}$, which corresponds to age, mass and radius uncertainties of ~ 10 , ~ 7 , and ~ 3 per cents respectively. These uncertainties account for observational errors and current state-of-the-art stellar models uncertainties. Our seismic study also provides constraints on surface convection properties, through the mixing-length that we find to be $12 - 15$ per cents smaller than the solar value. On the other hand, because of helium-mass degeneracy, the initial helium abundance is determined modulo the mass value. Finally, we evaluate the seismic mass of the exoplanet to be $M_p \sin i = 1.17 - 1.26 M_{\text{Jupiter}}$, much more precise than what can be derived by Hertzsprung-Russell diagram inversion.

Conclusions. We demonstrate that asteroseismology allows to substantially improve the age accuracy compared to other methods. We emphasize that the knowledge of the mean properties of stellar oscillations - as the large frequency separation - is not enough for deriving accurate ages. We need precise individual frequencies to narrow the age scatter due to uncertainties of models input physics. Further progress will require to better constrain the physics at work in stars and their helium content. Our results strengthen the case for precise classical stellar parameters and oscillation frequencies as will be obtained by the Gaia and PLATO missions.

Key words. asteroseismology - stars: interiors - stars: evolution - stars: oscillations - stars: individual: HD 52265 - stars: fundamental parameters - planets and satellites: fundamental parameters

1. Introduction

Stellar ages are crucial inputs in many astrophysical studies. For instance, the knowledge of the stellar formation rate and age-metallicity relation (Gilmore 1999; Hernandez et al. 2000) is essential to understand the formation and evolution of our Galaxy (Freeman 1993). Also, precise ages of the oldest galactic halo stars are essential to set a lower limit to the age of the Universe (Watson 1998). Moreover, the huge harvest of newly discovered exoplanets calls for accurate and precise ages of their host-stars, a crucial parameter in the understanding of planet formation and evolution (Havel et al. 2011).

While stellar masses and/or radii can be measured directly for some particular stars – masses and radii for members of binary systems, radii for giant stars or bright dwarfs observable in interferometry – stellar ages cannot be determined by direct measurements but can only be estimated or inferred. As reviewed by Soderblom (2010), there are many methods to estimate the age of a star according to its mass, evolutionary state

and configuration – single star or star in a group. The ages of single main sequence (MS) stars are often inferred from empirical indicators (activity or rotation) and/or from stellar model isochrones which are compared to observed, hereafter named, classical parameters – effective temperature T_{eff} , luminosity L or surface gravity $\log g$, and metallicity $[\text{Fe}/\text{H}]$. However the precision and accuracy currently reached are not good enough to characterize exoplanets precisely (Havel et al. 2011). Several error sources hamper single stars age-dating, namely the errors on the observational data, the internal error related to the age-dating method and, for stellar model dependent methods, the degree of realism of the models. Depending on the mass and evolutionary stage and on the method, the error on age maybe in the range 50 to more than 150 per cents (see for instance Lebreton & Montalbán 2009, and references therein).

Indeed, stellar models outputs, as the age attributed to a given star, are quite sensitive to the physical inputs of the models calculation. For instance, a major impact of the processes transporting or mixing chemical elements, as convection and over-

shooting, microscopic diffusion, and turbulent diffusion induced by hydrodynamical instabilities has been found. Unfortunately these processes are still not well described and often have to be parametrized.

Progress is seen with the availability of asteroseismic data provided by the high precision photometric missions CoRoT (Baglin et al. 2002) and Kepler (Koch et al. 2010). Low amplitude solar-like oscillations have been detected in a large amount of stars and their frequencies measured with a typical precision of a few tenths micro Hertz (e.g. Michel et al. 2008; Chaplin & Miglio 2013). Seismic data have been used recently and massively to age-date and weigh stars. Currently, two approaches are taken. The first one, ensemble asteroseismology, attempts to determine the mass and age of large sets of stars based on their mean seismic properties (Chaplin et al. 2014). In this approach, interpolation in large grids of stellar models, by different techniques, provides the mass and age of the model that best matches the observations. The alternative approach, more precise, is the here-after named “à la carte” modelling¹ (Lebreton 2013), that is, the detailed study of specific stars, one by one, also referred to as “boutique” modelling, (see e.g. D. Soderblom, 2013, invited review at the International Francqui Symposium²). This approach has been used to model CoRoT and Kepler stars (see the reviews by Baglin et al. 2013; Chaplin & Miglio 2013). Stars hosting exoplanets have been modelled by e.g. Gilliland et al. (2011); Lebreton (2012); Escobar et al. (2012); Lebreton (2013); Gilliland et al. (2013).

In the present study, we address the specific problem of the quantification of the sources of inaccuracy affecting the estimates of the age, mass, and radius of stars. In the past, Brown et al. (1994) addressed this problem theoretically while Lebreton et al. (1995) discussed it in an early prospective study related to the preparation of the Gaia-ESA mission. The need for such a quantification has become even more crucial because age, mass and radius of exoplanet host-stars are keys to characterize the planets and then to understand their formation and evolution. This is therefore a prerequisite in the context of space missions CoRoT, Kepler, and forthcoming Gaia, TESS, and PLATO. Recently, Valle et al. (2014) used a grid approach and a synthetic sample of solar-type MS stars to carry out a theoretical investigation in order to identify and quantify the sources of biases on the mass and radius determinations. Here we rather consider a “à la carte” approach to characterize a main CoRoT target, HD 52265, as an illustrative case-study. The G-type metal-rich star HD 52265 is a MS star which hosts an exoplanet -the transit of which was not observable- but CoRoT provided a rich solar-like oscillation spectrum that was analysed by Ballot et al. (2011) and Gizon et al. (2013). HD 52265 has been modelled by Soriano et al. (2007) prior to its observation by CoRoT, and then by Escobar et al. (2012) and Lebreton & Goupil (2012) on the basis of CoRoT data. The asteroseismic modelling by Escobar et al. (2012) was based on the large and small mean frequency separations (see Sect. 2). It provided a seismic mass of $1.24 \pm 0.02 M_{\odot}$, a seismic radius of $1.33 \pm 0.02 R_{\odot}$, and a seismic age of 2.6 ± 0.2 Gyr. Note that the error bars on these values do not include the impact of the uncertainties on stellar model inputs. Also, the mass of the exoplanet was not evaluated.

In this study, we have characterized the star in terms of age, mass, radius, initial helium content, etc. To that end, we have performed “à la carte” modelling based on several classes of

dedicated stellar models corresponding to different assumptions on the input physics and chemical composition, and we have used different sets of observational parameters to constrain the models. We have examined how the uncertainties on the observational constraints, and on the model input physics and free parameters impact the results of stellar modelling.

In Sect. 2, we review the observational data available for HD 52265. In Sect. 3, we describe our methodology and choices for cases of interest. The results are detailed in Sect. 4, namely the range of age, mass, radius, initial helium content, and mixing-length parameter of the models. They show how the use of seismic constraints severely restricts these ranges. For comparison, Sect. 5.1 discusses the empirical ages of the star, while Sect. 5.2 presents ages obtained through isochrone placement in the Hertzsprung-Russell (H-R) diagram. We discuss the impact of the uncertainty on the mass of the host-star on the exoplanet one in Sect. 6, and we draw some conclusions in Sect. 7.

2. Observational constraints for HD 52265

This section reviews the observational data that we used as constraints for the modelling of HD 52265.

2.1. Astrometry, photometry and spectroscopy

HD 52265 (HIP 33719) is a nearby single G0V star. According to its Hipparcos parallax $\pi = 34.53 \pm 0.40$ mas (van Leeuwen 2007) it is located at ≈ 29 pc. To model the star, we considered the observational data listed in Table 1. In the literature, we gathered twenty spectroscopic determinations of the effective temperature T_{eff} , surface gravity $\log g$, and metallicity $[\text{Fe}/\text{H}]$ of HD 52265 reported since 2001. We adopted here the average of these quantities and we derived the error bars from the extreme values reported. To derive the luminosity L , we used the parallax and the Tycho V_T magnitude, $V_T = 6.358 \pm 0.004$ mag, which we translated into the Johnson value, $V_J = 6.292 \pm 0.005$ mag, following Mamajek et al. (2002). The bolometric correction $BC = -0.014 \pm 0.012$ was derived from T_{eff} , $\log g$, and $[\text{Fe}/\text{H}]$ using the tools developed by Vandenberg & Clem (2003). The Stefan-Boltzmann radius corresponding to the adopted values of L and T_{eff} is $R_{\text{SB}} = 1.28 \pm 0.06 R_{\odot}$.

Butler et al. (2000) detected the presence of an exoplanet, through observed radial velocity (RV) variations of HD 52265. From the RV curve they derived the semi-amplitude K , orbital period P , eccentricity e and semi-major axis a of the orbit. From RV data and the Kepler third law, a lower limit on the mass of the planet can be inferred, via

$$M_p \sin i = M_{\text{star}}^{2/3} K (1 - e^2)^{1/2} (P/2\pi G)^{1/3} \quad (1)$$

where i is the angle of inclination of the orbital plane on the sky (see e.g. Perryman 2011). This will be further discussed in Sect. 6.

2.2. CoRoT light-curve inferences and seismic constraints

Ultra high-precision photometry of HD 52265, performed on-board CoRoT for four months, provided a light-curve carrying the signature of oscillations (Ballot et al. 2011).

2.2.1. Individual oscillation frequencies

HD 52265 shows a pressure-mode (p-mode) solar-like oscillation spectrum, in which Ballot et al. (2011) identified 28 reliable

¹ We use “à la carte” in opposition to “set meal” to stress the point that models are specifically fashioned to study a case-study star.

² <http://fys.kuleuven.be/ster/meetings/francqui>

Table 1. Main observational constraints for the modelling of HD 52265.

T_{eff} [K]	$\log g$ [dex]	[Fe/H] [dex]	L [L_{\odot}]	$\langle \Delta \nu \rangle$ [μHz]	$\Delta \nu_{\text{asym}}$ [μHz]	$\langle d_{02} \rangle$ [μHz]	$\langle r_{02} \rangle$ –	$\langle rr_{01/10} \rangle$ –
6116 ± 110	4.32 ± 0.20	0.22 ± 0.05	2.053 ± 0.053	98.13 ± 0.14	98.19 ± 0.05	8.20 ± 0.31	0.084 ± 0.003	0.033 ± 0.002

low-degree p-modes of angular degrees $\ell = 0, 1, 2$ and radial orders n in the range 14–24 (see their Table 4). The frequencies $\nu_{n,\ell}$ are in the range 1500–2550 μHz . Data being of high-quality, the precision on each frequency is of a few tenths of μHz .

In the present study, individual frequencies were used to constrain stellar models. Before turning to the issues related to the use of individual frequencies, we have to briefly recall some basic properties of stellar oscillations.

A formulation adapted from the asymptotic expansion by Tassoul (1980) is commonly used to interpret the observed low-degree oscillation spectra (see e.g. Mosser et al. 2013, and references therein). It approximates the frequency of a p-mode of high radial order n and angular degree $\ell \ll n$ as

$$\nu_{n,\ell} \simeq \left(n + \frac{1}{2}\ell + \epsilon \right) \Delta \nu_{\text{asym}} - \ell(\ell + 1)D_0 \quad (2)$$

where the coefficients ϵ , $\Delta \nu_{\text{asym}}$, D_0 depend on the considered equilibrium state of the star. In particular

$$\Delta \nu_{\text{asym}} = \left(2 \int_0^R \frac{dr}{c} \right)^{-1} \quad \text{and} \quad D_0 \approx -\frac{\Delta \nu_{\text{asym}}}{4\pi^2 \nu_{n,\ell}} \int_0^R \frac{dc}{r} \quad (3)$$

where c is the adiabatic sound speed $c = (\Gamma_1 P / \rho)^{1/2}$ (Γ_1 is the first adiabatic index, P the pressure, and ρ the density). For a perfect gas, $c \propto (T/\mu)^{1/2}$ where T is the temperature and μ the mean molecular weight.

The quantity $\Delta \nu_{\text{asym}}$ measures the inverse of the sound travel time across a stellar diameter and is proportional to the square of the mean density while D_0 probes the evolution status (and then age) through the sound speed gradient built by the chemical composition changes in the stellar core.

The ϵ term weakly depends on n and ℓ but it is much sensitive to the physics of surface layers. The problem is that outer layers in solar-type oscillators are the seat of inefficient convection, a 3-dimensional turbulent process, poorly understood. The modelling of near surface stellar layers is uncertain and so are the related computed frequencies. These so-called near-surface effects are a main concern when using individual frequencies to constrain stellar models because they are at the origin of an offset between observed and computed oscillation frequencies. Some empirical recipes can be used to correct for this offset. This will be further discussed in Sect. 3.2.

2.2.2. ν_{max} , $\langle \Delta \nu \rangle$ and scaling relations

From the oscillation power spectrum of HD 52265, Ballot et al. (2011) extracted the frequency at maximum amplitude $\nu_{\text{max}} = 2090 \pm 20 \mu\text{Hz}$. This quantity is proportional to the acoustic cut-off frequency, itself related to effective temperature and surface gravity (see e.g. Brown et al. 1994; Kjeldsen & Bedding 1995; Belkacem et al. 2011). This yields a scaling relation that can be used to constrain the mass and radius of a star of known T_{eff} ,

$$\nu_{\text{max,sc}} / \nu_{\text{max},\odot} = (M/M_{\odot})(T_{\text{eff}}/5777)^{-1/2}(R/R_{\odot})^{-2} \quad (4)$$

where $\nu_{\text{max},\odot} = 3050 \mu\text{Hz}$ is the solar value and the index “sc” stands for scaling.

The difference in frequency of two modes of same degree and orders differing by one unit reads

$$\Delta \nu_{\ell}(n) = \nu_{n,\ell} - \nu_{n-1,\ell} \quad (5)$$

and is named the large frequency separation. We used the mean large frequency separation to constrain stellar models and calculated it in three different ways but each time the observational value and the model value were calculated accordingly.

First, the mean large frequency separation can be calculated as an average of the individual separations defined by Eq. 5. We first calculated the mean separation $\langle \Delta \nu_{\ell} \rangle$ for each observed degree ($\ell = 0, 1, 2$), by averaging over the whole range of observed radial orders. We then obtained the overall mean separation from

$$\langle \Delta \nu \rangle = \frac{1}{3} \sum_{\ell=0}^2 \langle \Delta \nu_{\ell} \rangle. \quad \text{Its value is reported in Table 1.}$$

Second, in the asymptotic approximation (Eq. 2), $\Delta \nu_{\ell}(n) \equiv \Delta \nu_{\text{asym}}$ is approximately constant whatever the ℓ value. We carried out a weighted least-squares fit of the asymptotic relation, Eq. 2, to the 28 identified frequencies and got the value of $\Delta \nu_{\text{asym}}$ given in Table 2, as well as D_0 ($1.43 \pm 0.05 \mu\text{Hz}$) and ϵ (1.34 ± 0.01). The quoted error bars were inferred from a Monte Carlo simulation.

Third, as mentioned in Sect. 2.2.1, $\langle \Delta \nu \rangle \propto \langle \rho \rangle^{1/2}$. This yields a scaling relation usable to constrain stellar mass and radius (see e.g. Ulrich 1986; Kjeldsen & Bedding 1995),

$$\langle \Delta \nu \rangle_{\text{sc}} / \langle \Delta \nu \rangle_{\odot} = (M/M_{\odot})^{1/2} (R/R_{\odot})^{-3/2} \quad (6)$$

where $\langle \Delta \nu \rangle_{\odot} = 134.9 \mu\text{Hz}$.

The inversion of Eqs. 4 and 6, with the observed values of $\langle \Delta \nu \rangle$, ν_{max} and T_{eff} of Table 1, yields $R_{\text{sc}} = 1.33 \pm 0.02 R_{\odot}$, $M_{\text{sc}} = 1.25 \pm 0.05 M_{\odot}$ and $\log g_{\text{sc}} = 4.29 \pm 0.01$ dex.

2.2.3. Small frequency separations and separation ratios

The difference in frequency of two modes of degrees differing by two units and orders differing by one unit reads

$$d_{\ell, \ell+2}(n) = \nu_{n,\ell} - \nu_{n-1, \ell+2} \quad (7)$$

and is commonly referred to as the small frequency separation.

Modes of $\ell = 1$ are rather easy to detect while modes of $\ell = 2$ are not always observed or are affected by large error bars. This led Roxburgh & Vorontsov (2003) to propose to use the five points small separations $dd_{01}(n)$ and $dd_{10}(n)$ as diagnostics for stellar models. They read

$$dd_{01}(n) = \frac{1}{8}(\nu_{n-1,0} - 4\nu_{n-1,1} + 6\nu_{n,0} - 4\nu_{n,1} + \nu_{n+1,0}) \quad (8)$$

$$dd_{10}(n) = -\frac{1}{8}(\nu_{n-1,1} - 4\nu_{n,0} + 6\nu_{n,1} - 4\nu_{n+1,0} + \nu_{n+1,1}) \quad (9)$$

According to the asymptotic relation (Eq. 2), $d_{02}(n)$ scales as $\approx 6D_0$ while $dd_{01/10}(n)$ scale as $\approx 2D_0$. Thus, they all probe the evolutionary status of stars.

Furthermore, Roxburgh & Vorontsov (2003) demonstrated that while the frequency separations, here-before defined are

sensitive to near-surface effects, these effects nearly cancel in the frequency separation ratios defined as

$$r_{02}(n) = d_{02}(n)/\Delta\nu_1(n) \quad (10)$$

$$rr_{01}(n) = dd_{01}(n)/\Delta\nu_1(n); \quad rr_{10}(n) = dd_{10}(n)/\Delta\nu_0(n+1) \quad (11)$$

As detailed in the following, we used these frequency separations and ratios to constrain models of HD 52265. We denote by $\langle d_{02} \rangle$, $\langle r_{02} \rangle$ and $\langle rr_{01/10} \rangle$, the mean values of the small frequency separations and separation ratios here-before defined. To calculate the mean values given in Table 2, we averaged over the whole range of observed radial orders.

2.2.4. Related seismic diagnostics

Ulrich (1986) and Christensen-Dalsgaard (1988) proposed to use the couple $(\langle \Delta\nu \rangle, \langle d_{02} \rangle)$ as a diagnostic of age and mass of MS stars. To minimize near-surface physics the $(\langle \Delta\nu \rangle, \langle r_{02} \rangle)$ couple can be used instead (Oti Floranes et al. 2005).

The advantage of $\langle r_{02} \rangle$ is that it decreases regularly as evolution proceeds on the MS. But, when only modes of $\ell = 1$ are observed, it is interesting to consider the mean ratios $\langle rr_{01/10} \rangle$ which are also sensitive to age. This is illustrated in Fig. 1 that shows the run of $(\langle rr_{01} \rangle + \langle rr_{10} \rangle)/2$ as a function of $\langle \Delta\nu \rangle$ along the evolution on the MS of stars of different masses. For all masses, the $\langle rr_{01/10} \rangle$ ratio decreases at the beginning of the evolution on the MS down to a minimum and then increases up to the end of the MS. The minimum value is larger and occurs earlier as the mass of the star increases, i.e. as a convective core appears and develops.

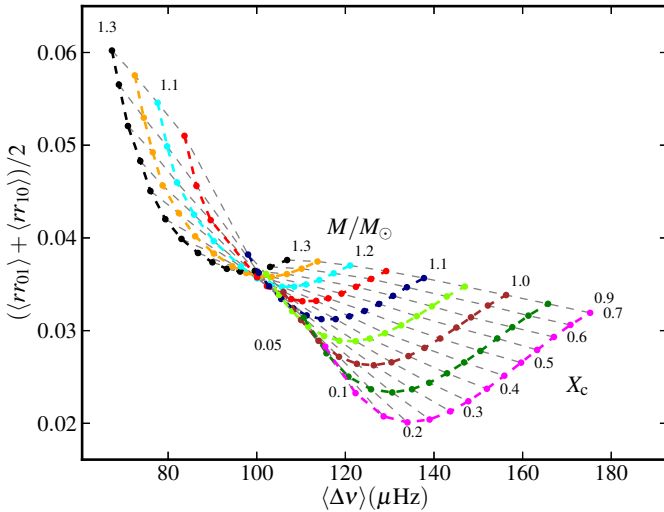


Fig. 1. Asteroseismic diagram showing the run of $(\langle rr_{01} \rangle + \langle rr_{10} \rangle)/2$ as a function of $\langle \Delta\nu \rangle$ for stars with masses in the range $0.9 - 1.3 M_{\odot}$ during the MS. Models have been calculated with an initial helium abundance $Y = 0.275$, solar metallicity $Z/X = 0.0245$ and mixing-length parameter $\alpha_{\text{conv}} = 0.60$. Evolutionary stages with decreasing central hydrogen abundance X_c are pin-pointed.

Deviations from the asymptotic theory are found in stars, as soon as steep gradients of physical quantities are built. This occurs for instance at the boundaries of convective zones due to the abrupt change of energy transport regime. Such

glitches impact the sound speed, and an oscillatory behaviour is then visible in frequency differences (see e.g. Gough 1990; Audard & Provost 1994; Roxburgh & Vorontsov 1994). In Lebreton & Goupil (2012), we used the oscillatory behaviour of the observed $rr_{01}(n)$ and $rr_{10}(n)$ ratios to estimate the amount of penetrative convection below the convective envelope of HD 52265.

2.2.5. Rotation period and inclination of the rotation axis

Ballot et al. (2011) derived a precise rotation period, $P_{\text{rot}} = 12.3 \pm 0.14$ days from the light-curve. Gizon et al. (2013) used seismic constraints to estimate the inclination of the spin axis of HD 52265 and found $\sin i = 0.59^{+0.18}_{-0.14}$. This allows to estimate the mass of the exoplanet detected by RV variations (Butler et al. 2000), under the standard assumption that the stellar rotation axis is the same as the axis of the exoplanet orbit (see Sect. 6).

3. Searching for an optimal model of HD 52265

We present the optimization method we used to obtain a model that best matches a selected set of observational constraints. We considered several choices of observational constraints, as explicated in Sect. 3.4. First, we chose a reference set of input physics for the modelling and, for this set, the optimization gave us a reference model for each selected case of observational constraints. In a second step, we carried out additional optimizations based on other possible choices for the input physics. We then quantified the age and mass uncertainties, for instance by comparing the extra models to the reference one. Hereafter, we first present the inputs of the models (Sect. 3.1), then the calculation of the oscillation frequencies (Sect. 3.2), and finally the optimization method (Sect. 3.3) and the choice of the sets of observational constraints (Sect. 3.4).

3.1. Models input physics and chemical composition

We have modelled the star with the stellar evolution code Cesam2k (Morel & Lebreton 2008; Marques et al. 2013). Following Lebreton et al. (2008), to ensure numerical accuracy, the models were calculated with ≈ 2000 mesh points and ≈ 100 time steps were taken to reach the optimized final model of the star. Our aim has been to evaluate the effect of the choice of the model input physics on the inferred age, mass and radius of HD 52265. We considered the input physics and parameters described below and listed in Table 2.

- **Opacities, equation of state (EoS), nuclear reaction rates:** Our reference models (set A, Table 2) are based on the OPAL05 EoS (Rogers & Nayfonov 2002) and on OPAL96 opacities (Iglesias & Rogers 1996) complemented at low temperatures by WICHITA tables (Ferguson et al. 2005). We used the NACRE nuclear reaction rates (Angulo et al. 1999) except for the $^{14}\text{N}(p, \gamma)^{15}\text{O}$ reaction where we adopted the revised LUNA rate (Formicola et al. 2004). To estimate uncertainties, we also calculated models based on the OPAL01 EoS (set H) and the NACRE nuclear reaction rate for the $^{14}\text{N}(p, \gamma)^{15}\text{O}$ reaction (set D).
- **Microscopic diffusion:** Our reference models take into account the microscopic diffusion of helium and heavy elements -including gravitational settling, thermal and concentration diffusion but no radiative levitation - following the formalism of Michaud & Proffitt (1993, hereafter MP93).

Note that Escobar et al. (2012) showed that radiative accelerations do not impact the structure of the models of HD 52265. To estimate uncertainties, we calculated models without diffusion (set *E*) and models with diffusion but treated with the Burgers (1969, hereafter B69) formalism (set *G*). In a test, we investigated the effect of mixing resulting from the radiative diffusivity associated to the kinematic radiative viscosity ν_{rad} (subset *A* described in Appendix A). According to Morel & Thévenin (2002), it can be modelled by adding an extra mixing diffusion coefficient $d_{\text{rad}} = D_R \times \nu_{\text{rad}}$ with $D_R \approx 1$. It limits gravitational settling in the outer stellar layers of stars with thin convective envelopes.

- **Convection:** Our reference is the CGM convection theory of Canuto et al. (1996) which includes a free mixing-length parameter $\alpha_{\text{conv}} = \ell/H_p$ (ℓ is the mixing-length and H_p the pressure scale height). To estimate uncertainties, we considered, in set *B*, the MLT theory (Böhm-Vitense 1958). When enough observational constraints are available, the value of α_{conv} is derived from the optimization of the models. When not enough observational constraints are available, the value of the mixing length has to be fixed. For the reference model, it is fixed to the solar value $\alpha_{\text{conv,CGM}} = 0.688$ or $\alpha_{\text{conv,MLT}} = 1.762$, i.e. resulting from the calibration of the radius and luminosity of a solar model with the same input physics (see e.g. Morel & Lebreton 2008). Other choices for the mixing length are considered in the study and presented in Appendix A.
- **Core overshooting:** In reference models we did not consider overshooting. We explored its impact in alternate models where we assumed that the temperature gradient in the overshooting zone is adiabatic. A first option (set *I*) was to set the core overshooting distance to be $\ell_{\text{ov,c}} = \alpha_{\text{ov}} \times \min(R_{\text{cc}}, H_p)$ where R_{cc} is the radius of the convective core and $\alpha_{\text{ov}} = 0.15$. In a second option (set *J*), we adopted the Roxburgh (1992) prescription, in which overshooting extends on a fraction of the mass of the convective core M_{cc} , the mass of the mixed core being expressed as $M_{\text{ov,c}} = \alpha_{\text{ov}} \times M_{\text{cc}}$ with $\alpha_{\text{ov}} = 1.8$.
- **Penetrative convection:** Convective penetration below the convective envelope is the penetration of fluid elements into the radiative zone due to their inertia. It leads to efficient convective heat transport with penetrative flows that establish a close to adiabatic temperature gradient, and to an efficient mixing of material in the extended region. A model for penetrative convection has been designed by Zahn (1991). In this model, the distance of fluid penetration into the radiative zone reads $L_p = \frac{\xi_{\text{PC}}}{\chi_P} H_p$ where $\chi_P = (\partial \log \chi / \partial \log P)_{\text{ad}}$ is the adiabatic derivative with respect to pressure P of the radiative conductivity $\chi = \frac{16\sigma T^3}{3\rho\kappa}$ (κ and σ are the opacity and Stefan-Boltzmann constant, respectively). The free parameter ξ_{PC} is of the order of unity but has to be calibrated from the observational constraints. We adopted here either $\xi_{\text{PC}} = 0.0$ (reference Set A, no penetration) or $\xi_{\text{PC}} = 1.3$ (set *K*), this latter best adjusts the oscillatory behaviour of the individual frequency separations $rr_{01/10}(n)$ of HD 52265 (Lebreton & Goupil 2012).
- **Rotation:** We did not include rotational mixing in our models, except in one test case (see subset A in Appendix A) where we considered rotation and its effects on the transport of angular momentum and chemicals as described in Marques et al. (2013). In that case, additional free coefficients enter the modelling, namely a coefficient K_w intervenes in the treatment of magnetic braking by stellar winds (see Eq. 9 in Marques et al. 2013), following the relation by

Kawaler (1988). We adjusted K_w so that the final model has the observed rotation period. This is one option among many possible ones. A thorough study of the impact of rotation on the modelling of HD 52265 will be presented in a forthcoming paper.

- **Atmospheric boundary condition:** The reference models are based on grey model atmospheres with the classical Eddington T- τ law. In set *F*, we investigated models based on the Kurucz (1993) T- τ law. For consistency with these Kurucz (1993) T- τ tables, in models *F* convection is computed according to the MLT theory.
- **Solar mixture** We adopted the canonical GN93 mixture (Grevesse & Noels 1993) as the reference but we considered the AGSS09 solar mixture (Asplund et al. 2009) in set *C*. The GN93 mixture $(Z/X)_{\odot}$ ratio is 0.0244 while the AGSS09 mixture corresponds to $(Z/X)_{\odot} = 0.0181$.
- **Stellar chemical composition:** The mass fractions of hydrogen, helium and heavy elements are denoted by X , Y and Z respectively. The present (Z/X) ratio is related to the observed $[\text{Fe}/\text{H}]$ value through $[\text{Fe}/\text{H}] = \log(Z/X) - \log(Z/X)_{\odot}$. We took a relative error of 11 per cents on $(Z/X)_{\odot}$ (Anders & Grevesse 1989). The initial $(Z/X)_0$ ratio is derived from model calibration as explained below.
For the initial helium abundance Y_0 we considered different possibilities. When enough observational constraints are available, the value of Y_0 is derived from the optimization of the models. When not enough observational constraints are available, the value of Y_0 has to be fixed. For the reference model, we derived it from the helium to metal enrichment ratio $(Y_0 - Y_p)/(Z - Z_p) = \Delta Y / \Delta Z$ where Y_p and Z_p are the primordial abundances. We adopted $Y_p = 0.245$ (e.g. Peimbert et al. 2007), $Z_p = 0$. and, $\Delta Y / \Delta Z \approx 2$, this latter from a solar model calibration in luminosity and radius. Other choices for Y_0 are considered in the study and presented in Appendix A.
- **Miscellaneous:** Impact of several alternate prescriptions for the free parameters are investigated and described in Appendix A.

3.2. Calculation of oscillation frequencies

We used the Belgium LOSC adiabatic oscillation code (Scuflaire et al. 2008) to calculate the frequencies. Frequencies and frequency differences were calculated for the whole range of observed orders and degrees. The observed and computed seismic indicators defined in Sect. 2 were derived consistently.

As mentioned in Sect. 2, near-surface effects are at the origin of an offset between observed and computed oscillation frequencies. We investigated the impact of correcting the computed frequencies from these effects. For that purpose, in some models (presented in Section 3.4 below), we applied to the computed frequencies, the empirical corrections obtained by Kjeldsen et al. (2008) from the seismic solar model:

$$\nu_{n,l}^{\text{mod,corr}} = \nu_{n,l}^{\text{mod}} + \frac{a_{\text{SE}}}{r_{\text{SE}}} \left(\frac{\nu_{n,l}^{\text{obs}}}{\nu_{\text{max}}} \right)^{b_{\text{SE}}} \quad (12)$$

where $\nu_{n,l}^{\text{mod,corr}}$ is the corrected frequency, $\nu_{n,l}^{\text{mod}}$ and $\nu_{n,l}^{\text{obs}}$ are respectively the computed and observed frequency, b_{SE} is an adjustable coefficient, r_{SE} gets close to unity when the model approaches the best solution and a_{SE} is deduced from the values of b_{SE} and r_{SE} . We followed the procedure of Brandão et al.

Table 3. Summary of the different cases considered for the modelling of HD 52265. A and M stand for age and mass respectively.

Case	Observed	Adjusted	Fixed
1	$T_{\text{eff}}, L, [\text{Fe}/\text{H}]$	A, M, $(Z/X)_0$	$\alpha_{\text{conv}}, Y_0$
2a, b, c	$T_{\text{eff}}, L, [\text{Fe}/\text{H}], \langle \Delta\nu \rangle$	A, M, $(Z/X)_0, \alpha_{\text{conv}}$	Y_0
3	$T_{\text{eff}}, L, [\text{Fe}/\text{H}], \langle \Delta\nu \rangle, \nu_{\text{max}}$	A, M, $(Z/X)_0, \alpha_{\text{conv}}, Y_0$	—
4	$T_{\text{eff}}, L, [\text{Fe}/\text{H}], \langle \Delta\nu \rangle, \langle d_{02} \rangle$	A, M, $(Z/X)_0, \alpha_{\text{conv}}, Y_0$	—
5	$T_{\text{eff}}, L, [\text{Fe}/\text{H}], \langle r_{02} \rangle, \langle rr_{01/10} \rangle$	A, M, $(Z/X)_0, \alpha_{\text{conv}}, Y_0$	—
6	$T_{\text{eff}}, L, [\text{Fe}/\text{H}], r_{02}(n), rr_{01/10}(n)$	A, M, $(Z/X)_0, \alpha_{\text{conv}}, Y_0$	—
7	$T_{\text{eff}}, L, [\text{Fe}/\text{H}], \nu_{n,\ell}$	A, M, $(Z/X)_0, \alpha_{\text{conv}}, Y_0$	—

Table 2. Summary of the different sets of input physics considered for the modelling of HD 52265. As detailed in the text, the reference set of inputs denoted by REF is based on OPAL05 EoS, OPAL96/WICHTA opacities, NACRE+LUNA reaction rates (this latter only for $^{14}\text{N}(p, \gamma)^{15}\text{O}$), the CGM formalism for convection, the MP93 formalism for microscopic diffusion, the Eddington grey atmosphere and GN93 solar mixture and includes neither overshooting, nor convective penetration or rotation. For the other cases we only indicated the input that is changed with respect to the reference. The colours and symbols in column 3 are used in Figs. 4 to 6, and in Fig. 9, but note that the colour symbols used in Fig. 3 are unrelated.

Set	Input physics	Figure symbol/colour
A	REF	circle, cyan
B	convection MLT	square, orange
C	AGSS09 mixture	diamond, blue
D	NACRE for $^{14}\text{N}(p, \gamma)^{15}\text{O}$	small diamond, magenta
E	no microscopic diffusion	pentagon, red
G	B69 for microscopic diffusion	upwards triangle, chartreuse
F	Kurucz model atmosphere, MLT	bowtie, brown
H	EoS OPAL01	downwards triangle, purple
I	overshooting $\alpha_{\text{ov}}=0.15H_p$	inferior, yellow
J	overshooting $M_{\text{ov,c}}=1.8 \times M_{\text{cc}}$	superior, gold
K	penetrative convection $\xi_{\text{PC}}=1.3H_p$	asterisk, pink

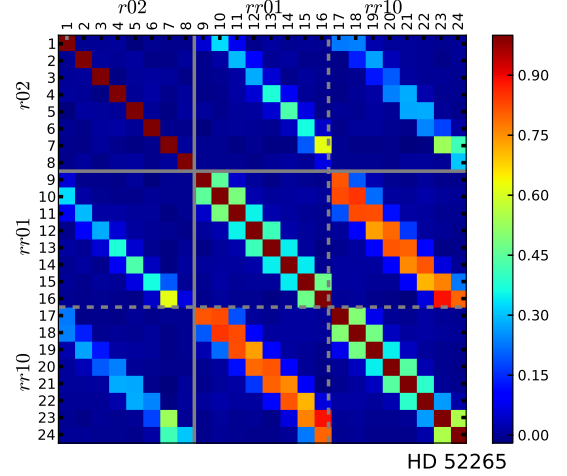
(2011). Kjeldsen et al. obtained a value of $b_{\text{SE},\odot} = 4.9$ when adjusting the relation on solar radial modes frequencies. However the value of $b_{\text{SE},\odot}$ should depend on the input physics in the solar model considered. Indeed, Deheuvels & Michel (2011) obtained $b_{\text{SE},\odot} = 4.25$ for a solar model computed with the CEsam2k code and adopting the CGM instead of MLT description of convection. Furthermore, b_{SE} could differ from one star to another. Under these considerations, we treated b_{SE} as a variable parameter of the modelling that we adjusted in the range [3.5, 5.5] so as to minimize the differences between observed and computed individual frequencies (see also Gruberbauer et al. 2012).

3.3. Model optimization

We used the Levenberg-Marquardt minimization method in the way described by Miglio & Montalbán (2005) to adjust the free parameters of the modelling so that models of HD 52265 match at best observations, within the error bars. The goodness of the match is evaluated through a χ^2 -minimization. We calculated

$$\chi^2 = \sum_{i=1}^{N_{\text{obs}}} \frac{(x_{i,\text{mod}} - x_{i,\text{obs}})^2}{\sigma_{i,\text{obs}}^2} \quad \text{and} \quad \chi_{\text{R}}^2 = \frac{1}{N_{\text{obs}}} \cdot \chi^2 \quad (13)$$

where N_{obs} is the total number of observational constraints considered, $x_{i,\text{mod}}$ and $x_{i,\text{obs}}$ are the computed and observed values of the i^{th} constraint, respectively, and χ_{R}^2 a reduced value. We

**Fig. 2.** Elements of the correlation matrix of the observed ratios $r_{02}(n)$ and $rr_{01/10}(n)$. Lines (columns) 1 to 8 correspond to the $r_{02}(n)$ ratios (n is in the range 17-24). Lines (columns) 9 to 16 correspond to the $rr_{01}(n)$ ratios and lines (columns) 17 to 24 correspond to the $rr_{10}(n)$ ratios (n is in the range 16-23). As expected, there are strong correlations between some of the data, in particular between the $rr_{01}(n)$ and $rr_{10}(n)$ ratios having the same n value or values of n differing by one unit.

distinguished χ_{classic}^2 based on the classical parameters and χ_{seism}^2 based on the seismic parameters. The more observational constraints available, the more free parameters can be adjusted in the modelling process. If too few observational constraints are available, some free parameters have to be fixed (see below). Accordingly, seven optimization cases were considered, as listed in Table 3 and described in Sect. 3.4 below.

In the cases where we considered the constraints brought by individual separations ratios $r_{02}(n)$ and $rr_{01/10}(n)$, we had to take into account the strong correlations between the ratios. To evaluate the correlations, we drew random samples of 20,000 values of each individual frequency assuming the errors on the frequencies are Gaussian and then we calculated the corresponding ratios and the associated covariance matrix C , displayed in Fig. 2. In this case, the χ^2 was calculated as

$$\chi^2 = \sum_{i=1}^{N_{\text{obs}}} (x_{i,\text{mod}} - x_{i,\text{obs}})^T \cdot C^{-1} \cdot (x_{i,\text{mod}} - x_{i,\text{obs}}) \quad (14)$$

where T denotes a transposed matrix (Press et al. 2002).

3.4. Choice of the set of observational constraints

We hereafter describe the various situations considered where N_{par} unknown parameters of a stellar model are adjusted to

fit N_{obs} observational constraints. We considered the following cases, summarized in Table 3. For each case we made one model optimization with each set of input physics listed in Table 2. We recall that the mean values of the frequency separations –either observed or theoretical– mentioned in the following were computed similarly as explained in Sect. 2.2.4.

1. Case 1: Age and mass from classical parameters.

In this case, we supposed that solely the classical parameters are constrained by observation (T_{eff} , present surface $[\text{Fe}/\text{H}]$, L). We sought which mass M , age A , and initial metal to hydrogen ratio $(Z/X)_0$ are required for the model to match these constraints. Since this gives 3 unknowns for 3 observed parameters, we made assumptions on the other inputs of the models, mainly the initial helium abundance Y_0 , the mixing-length α_{conv} , and overshooting parameter α_{ov} . As a reference, we assumed that Y_0 can be derived from the helium to metal enrichment ratio $\Delta Y/\Delta Z = 2$. We took $\alpha_{\text{conv},\odot}=0.688$ from solar model calibration and $\alpha_{\text{ov}}=0.0$. Other models, presented in Appendix A, consider extreme values of Y_0 (the primordial, minimum allowed value, 0.245), of α_{conv} (0.550, 0.826, i.e. a change in $\alpha_{\text{conv},\odot}$ by 20 per cents) and of α_{ov} (0.30).

2. Cases 2a, b, c: Age and mass from large frequency separation $\langle\Delta\nu\rangle$ and classical parameters.

In this case, we supposed that only $\langle\Delta\nu\rangle$ is known together with the classical parameters. We could then adjust the mixing-length parameter, together with the mass, age and initial metal to hydrogen ratio (4 unknowns, 4 constraints). We still had to fix the initial helium abundance from $\Delta Y/\Delta Z$. We considered three sub-cases.

In sub-case 2a, we did not explicitly calculate the frequencies of the model but derived the model large frequency separation from the scaling relation (Eq. 6) and compared to the observed mean large frequency separation $\langle\Delta\nu\rangle$ of Table 1. In sub-case 2b, we estimated the theoretical $\langle\Delta\nu\rangle$ from the computed set of individual frequencies and compared to the observed $\langle\Delta\nu\rangle$. In sub-case 2c, we adjusted the computed $\Delta\nu_{\text{asym}}$ (Eq. 2) to the observed one in Table 1. In Cases 2b and 2c, we corrected the model frequencies from near-surface effects according to Eq. 12.

3. Case 3: Age and mass from scaled values of $\langle\Delta\nu\rangle$ and ν_{max} , and classical parameters.

This case is similar to Case 2a with the additional constraint on ν_{max} from the scaling relation (Eq. 4). Frequencies are not explicitly calculated in this case.

4. Case 4: Age and mass from large frequency separation $\langle\Delta\nu\rangle$, mean small frequency separation $\langle d_{02}\rangle$ and classical parameters.

In this case the frequencies are explicitly calculated and corrected from near-surface effects according to Eq. 12. The model $\langle\Delta\nu\rangle$ and $\langle d_{02}\rangle$ are compared to observed values of Table 1.

5. Cases 5 and 6: Age and mass from frequency separations ratios $-r_{02}$, $rr_{01/10}$ – and classical parameters.

In both cases the frequencies are explicitly calculated. In Case 5, the mean values of r_{02} , $rr_{01/10}$ were calculated and compared to observed values of Table 1. In Case 6, we used the observed individual ratios $r_{02}(n)$, $rr_{01/10}(n)$ to constrain the models. Since the use of r_{02} , $rr_{01/10}$ allows to minimise the impact of near-surface effects (Roxburgh & Vorontsov 2003), we used uncorrected ratios. On the other hand, we always accounted for observed data correlations. However, a model neglecting these correlations was calculated which

shows that they do not impact the results very much (see Appendix A). In the Appendix, we also discuss the point made by Roxburgh & Vorontsov (2013), on the correct way to extract, from a model, the frequency separation ratios to be compared with observed ones.

6. Case 7: Age and mass from individual frequencies $\nu_{n,\ell}$ and classical parameters.

In this case, we considered the full set of 28 frequencies as constraints and corrected the model frequencies according to Eq. 12 where we adjusted b_{SE} to minimise the χ^2 . In Appendix A, we evaluated the differences obtained when no correction of near-surface effects is applied or when the surface effects are corrected using the Kjeldsen et al. (2008) solar value of the b_{SE} parameter ($b_{\text{SE},\odot} = 4.90$).

4. Results of “à la carte” stellar modelling

The inputs and results of the different models presented in Sect. 3 are listed in Tables 4 and 5 for the reference models (Set A, Table 2). Table 4 lists the quantities that are usual main inputs of stellar models and which can be determined by the optimization –or not– depending on the number of available observational constraints (see Table 3). Table 5 lists quantities that are usual outputs of a model calculation, some of them may also be observational constraints. For purpose of clearness, we chose to present further results in Appendix A. In Tables A.1, A.2 and A.3, the results of model optimization for different options in the calculation of reference models of Set A are given. In Tables A.4 and A.5, the results of model optimization for the input physics listed in Table 2 are presented. The data in Tables 4, 5, A.2, A.3, A.4, and A.5 are available at <http://mygepi.obspm.fr/~lebreton/Modeles/CESAM.html>, in ASCII format.

The reduced values (χ_R^2) are also given to show the goodness of the match. Depending on the optimization case, there may be orders of magnitude differences in the χ_R^2 -values. For instance, in Cases 1, the χ_R^2 -values are very small because it is quite easy to find a model that matches the classical parameters only. Hence, *in Cases 1, for a given set of input physics and fixed free parameters, the optimization provides a very precise solution but the stellar model may not be accurately determined.* The adopted values of the fixed parameters such as the mixing length may not be appropriate for the studied star, this introduces biases which can have strong impact on the results as discussed below. *On the other hand, in the other cases, seismology puts severe constraints on the models which results in larger χ_R^2 -values. The result is then less precise but the stellar model is more accurate.* Note that at this point we listed all models whatever their χ_R^2 -value.

4.1. Observational constraints restitution

To each of the 9 sets of observational constraints presented in Table 3 corresponds 11 different models optimized with the input physics listed in Table 2. Figures 3 illustrate how the observational constraints of HD 52265 listed in Table 1 are reproduced by these models.

First, we examine the classical observables T_{eff} , L , $[\text{Fe}/\text{H}]$, and $\log g$. We consider two diagrams, a $T_{\text{eff}}-L$ and a $[\text{Fe}/\text{H}]-\log g$ diagram, as plotted in the upper left and right panels of Figs. 3. For purpose of readability we distinguish each set in Table 3 but not the different input physics in Table 2. These latter will be discussed in next sections. The total size of these diagrams is

Table 4. Model results for the reference physics (set A, different cases, see Sect. 3 and Tables 2 and 3). The uncertainties result from the Levenberg-Marquardt minimization procedure (i.e. diagonal terms of the covariance matrix of inferred parameters). No uncertainty is indicated when the parameter has not been inferred but fixed (not enough observational constraints as in Cases 1 and 2a, b, c). Note that to have homogeneous tables here and in the Appendix A, we give a column listing the values of α_{ov} and ξ_{PC} although there are equal to 0 in reference set A.

Model	Age (Gyr)	M/M_{\odot}	$(Z/X)_0$	Y_0	α_{conv}	α_{ov} / ξ_{PC}	b_{SE}	a_{SE}/r_{SE}	$\chi^2_{R,classic} / \chi^2_{R,seism}$
A1	2.90± 1.09	1.18± 0.02	0.0483±0.0051	0.311	0.688	0.00/0.00	–	–	6.4 10 ⁻⁷ / –
A2a	2.38± 0.88	1.19± 0.02	0.0493±0.0049	0.312	0.596±0.100	0.00/0.00	–	–	1.3 10 ⁻¹ /7.9 10 ⁻⁵
A2b	1.81± 0.80	1.20± 0.02	0.0491±0.0052	0.312	0.559±0.093	0.00/0.00	5.5	-4.5/1.00	1.2 10 ⁻¹ /2.6 10 ⁻⁴
A2c	1.97± 0.90	1.20± 0.02	0.0486±0.0053	0.311	0.575±0.086	0.00/0.00	5.5	-4.3/1.00	2.3 10 ⁻¹ /1.6 10 ⁻³
A3	1.98± 1.05	1.23± 0.01	0.0487±0.0055	0.298±0.020	0.565±0.102	0.00/0.00	–	–	2.6 10 ⁻¹ /1.7 10 ⁻²
A4	2.08± 0.27	1.13± 0.03	0.0509±0.0055	0.350±0.021	0.581±0.024	0.00/0.00	5.5	-4.7/1.00	2.4 10 ⁻³ /4.2 10 ⁻⁵
A5	2.17± 0.32	1.25± 0.05	0.0467±0.0061	0.280±0.038	0.671±0.093	0.00/0.00	–	–	3.3 10 ⁻⁷ /4.0 10 ⁻³
A6	2.21± 0.11	1.22± 0.02	0.0502±0.0024	0.299±0.011	0.599±0.031	0.00/0.00	–	–	1.7 10 ⁻¹ /8.5 10 ⁻¹
A7	2.17± 0.02	1.27± 0.00	0.0486±0.0007	0.274±0.001	0.601±0.004	0.00/0.00	4.2	-5.1/1.00	5.3 10 ⁻¹ /1.7 10 ⁰

Table 5. Model restitution of the chosen observational constraints plus quantities of interest. Models listed here were optimized with the reference physics (set A, different cases, see Sect. 3 and Tables 2 and 3). As explained in the text, in Cases 2b, 2c, 4 and 7 the optimization considers individual frequencies and separations that were corrected from near-surface effects while in Cases 5 and 6 the optimization is based on non-corrected separation ratios r_{02} and $rr_{01/10}$. In Case 1 no seismic constraints are considered. In Cases 1, 5 and 6, we nevertheless chose to list below a corrected value of $\langle\Delta\nu\rangle$, i.e. a value corrected for surface effects a posteriori, once the optimized model has been obtained. In Cases 2a and 3, the scaling values of $\langle\Delta\nu\rangle$ are given while in Case 2c, we list $\Delta\nu_{asym}$. Models with non reference options are presented in the Appendix.

Model	T_{eff} [K]	L [L_{\odot}]	[Fe/H] [dex]	log g [dex]	R [R_{\odot}]	$\langle\Delta\nu\rangle$ [μHz]	ν_{max} [μHz]	$\langle r_{02} \rangle$ –	$\langle rr_{01/10} \rangle$ –	X_C –	$\Delta Y/\Delta Z$ –	M_{cc} [M_{\star}]	R_{zc} [R_{\star}]	$M_p \sin i$ [$M_{Jupiter}$]
A1	6116.	2.053	0.22	4.29	1.28	101.33	2127.	0.074	0.033	0.28	2.0	0.032	0.767	1.17±0.03
A2a	6050.	2.063	0.22	4.28	1.31	98.13	2061.	0.081	0.034	0.33	2.0	0.024	0.798	1.18±0.03
A2b	6053.	2.063	0.22	4.28	1.31	98.14	2089.	0.088	0.035	0.40	2.0	0.019	0.819	1.19±0.03
A2c	6067.	2.082	0.21	4.28	1.31	98.26	2083.	0.086	0.034	0.38	2.0	0.021	0.813	1.19±0.03
A3	6024.	2.066	0.22	4.28	1.32	98.15	2086.	0.086	0.034	0.39	1.5	0.017	0.813	1.20±0.03
A4	6110.	2.055	0.22	4.28	1.28	98.13	2035.	0.084	0.035	0.33	3.3	0.035	0.809	1.14±0.03
A5	6116.	2.053	0.22	4.32	1.28	104.16	2253.	0.083	0.033	0.38	1.0	0.011	0.785	1.22±0.05
A6	6043.	2.081	0.23	4.29	1.32	98.29	2095.	0.083	0.034	0.37	1.5	0.021	0.801	1.20±0.03
A7	6020.	2.102	0.23	4.29	1.34	98.29	2124.	0.084	0.034	0.39	0.8	0.014	0.800	1.23±0.03

the size of the 2σ error box on the classical parameters while the inner box identifies the 1σ error box. The figures show that all models satisfy the classical constraints at the 2σ level with only two models lying outside the 1σ error box on T_{eff} , L , [Fe/H], and log g. These outliers are model E6 ([Fe/H]=0.28, no microscopic diffusion) and model K6 ($L/L_{\odot} = 2.12$, penetrative convection). It is worth to point out that models optimized with seismic data (especially the Cases 6 and 7 models) show a trend towards the lower range of the observed spectroscopic effective temperature. This strengthens the case for a redetermination of the observed T_{eff} at the light of the seismic surface gravity which is robust, as discussed below.

The seismic value for log g is found mostly independent of the model input physics (see also Sect. 4.4) and differs from the spectroscopic one by 0.03 dex. Note that two models have a log g in the upper range of the spectroscopic error bar, i.e. higher and farther from the seismic value. These are the two models of Case 5 with overshooting (I5 and J5). However, as discussed below, these models will not be considered in the following (model I5 has a very low initial helium content, much lower than the primordial value while model J5 has a high $\chi^2_{R,seism}$).

Second, we examine the seismic mean observables $\langle\Delta\nu\rangle$, $\langle r_{02} \rangle$, and $\langle rr_{01/10} \rangle$. We consider two diagrams, a $\langle\Delta\nu\rangle$ – $\langle r_{02} \rangle$ and a $\langle\Delta\nu\rangle$ – $\langle rr_{01/10} \rangle$ diagram, as plotted in the lower left and right panels of Figs. 3. Here, the total size of these diagrams is the size of the 10σ error box on the seismic parameters while two inner boxes delimit the 1σ and 3σ error boxes. We note that many

models lie outside the 1σ error box of $\langle\Delta\nu\rangle$, $\langle r_{02} \rangle$, and $\langle rr_{01/10} \rangle$. Some models are even not in the plotted areas. In most of these cases, the seismic data have not been used as model constraints. *In particular no model of Case 1 matches seismic constraints. This shows that a model which only matches the classical parameters can indeed be very far from a seismic model.*

We also note that several models in Tables 5, A.3, A.5 have ν_{max} -values well outside the 1σ range of the observational determination of Ballot et al. (2011) (we recall that Case 3 models have been optimized on ν_{max}). This can be explained by the fact that the error bar on ν_{max} given by Ballot et al. is an internal error which is quite small (1 per cent). As shown by Barban et al. (2013), the method adopted to infer ν_{max} from the power spectra impacts its value. Furthermore, one can expect differences between the observational value of ν_{max} and the theoretical value which obeys the scaling relation (e.g. Belkacem et al. 2013).

In the following, to derive the age and mass of HD 52265 and their uncertainties, we will consider only the models that satisfy $\chi^2_{R,classic} < 1$. Due to the high precision of the frequencies, no model with $\chi^2_{R,seism} < 1$ is found. We therefore only kept models with $\chi^2_{R,seism} < 2$.

4.2. Age of HD 52265

Figure 4 (left panel) shows for each case in Table 3, the age of the optimal model for a given set of physics in Table 2.

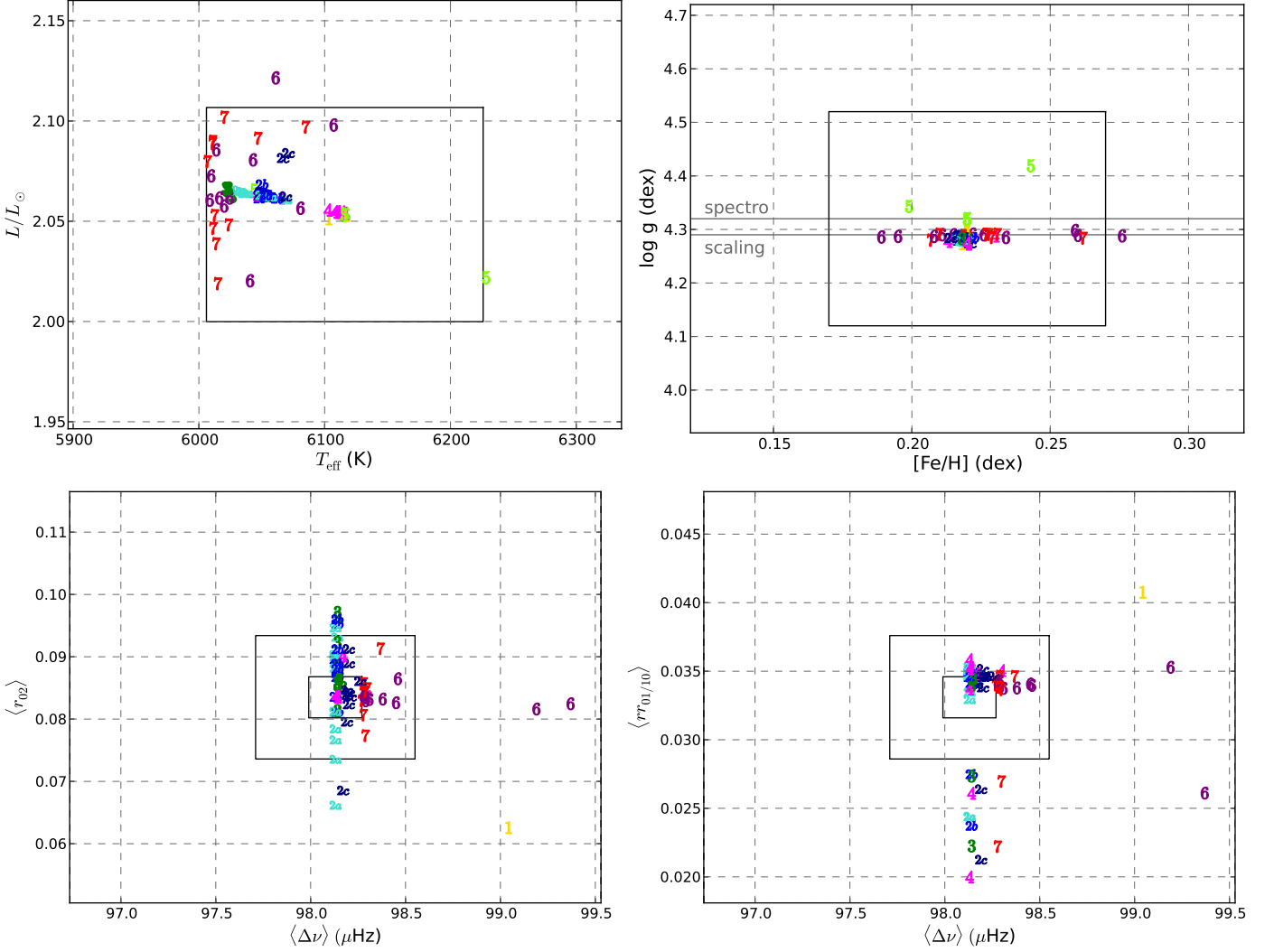


Fig. 3. Restoration of the observational constraints in the models. Upper figures are for classical parameters: HR-diagram (left), [Fe/H]-log g plane (right). The inner rectangle delimits the 1σ observational error bars and the boundaries of the whole plotting area represent 2σ errors. Horizontal lines give the log g values of spectroscopy and seismic scaling. Lower figures are for seismic indicators: $\langle \Delta\nu \rangle$ - $\langle r_{02} \rangle$ plane (left) and $\langle \Delta\nu \rangle$ - $\langle rr_{01/10} \rangle$ plane, (right). Here, the rectangles delimit 1 and 3σ error bars and the boundaries of the whole plotting area are 10σ errors. For each point, the symbol corresponds to the model number as explicated in Table 3. We used different colours to highlight the different cases (sets of observational constraints as defined in Table 3) at the basis of the modelling. Note that these colours are unrelated to the colours defined in Table 2 and used in Figs. 4 to 6, and in Fig. 9.

In Case 1 (respectively 2), Y and α_{conv} (respect. Y) could not be inferred and had to be fixed by the modeller. Therefore, for these two cases, we calculated additional models with somewhat extreme choices of Y and α_{conv} . In Case 1, we also included a model with a large amount of overshooting ($\alpha_{\text{ov}} = 0.30$). These extra models, included in Fig. 4, are presented in Appendix A.2.

In Case 1 (column 1 in Fig. 4), there is a large scatter in the ages of HD 52265 obtained with different sets of input physics when no seismic observations are available, i.e. $\approx \pm 60$ per cents with respect to the reference age. This is the usual situation of age-dating from classical parameters L , T_{eff} and surface [Fe/H]. The values of Y , α_{conv} , and α_{ov} had to be fixed and different ages result from different choices. In particular, for a change of α_{conv} of 20 per cents around the solar calibrated value, the age changes by more than 50 per cents. At the highest boundary of the age interval, the oldest models are those without diffusion and the model with a high mixing length $\alpha_{\text{conv}} = 0.826$. The youngest models are models with the smallest –primordial– initial helium

abundance ($Y_{\text{p}} = 0.245$) and the model with low $\alpha_{\text{conv}} = 0.55$. The ages of the other models are concentrated in a narrow age interval, 2.6-3.0 Gyr, about that of reference model A.

It is worth to point out that if the error bars on the classical parameters were to be reduced, as will be the case after the Gaia-ESA mission (see e.g. Liu et al. 2012, and references therein), the error bar of an individual age determination with a given set of input physics would be reduced but *the scatter associated to the use of different input physics would remain the same unless significant advances in stellar modelling are carried out.*

In Cases 2a, b, c where the large frequency separation is included as a model constraint, the age scatter is reduced with respect to Case 1. Unlike Case 1, the ages of the optimal models computed with different input physics and free parameters span the whole range of the scattered interval. Indeed, the values of the inferred mixing length differ from one case to another and still span a large range (0.466-0.656) for $\alpha_{\text{conv, cgm}}$ for Case 2a for instance, as can be seen in Tables 4, A.2, and A.4). Also, the

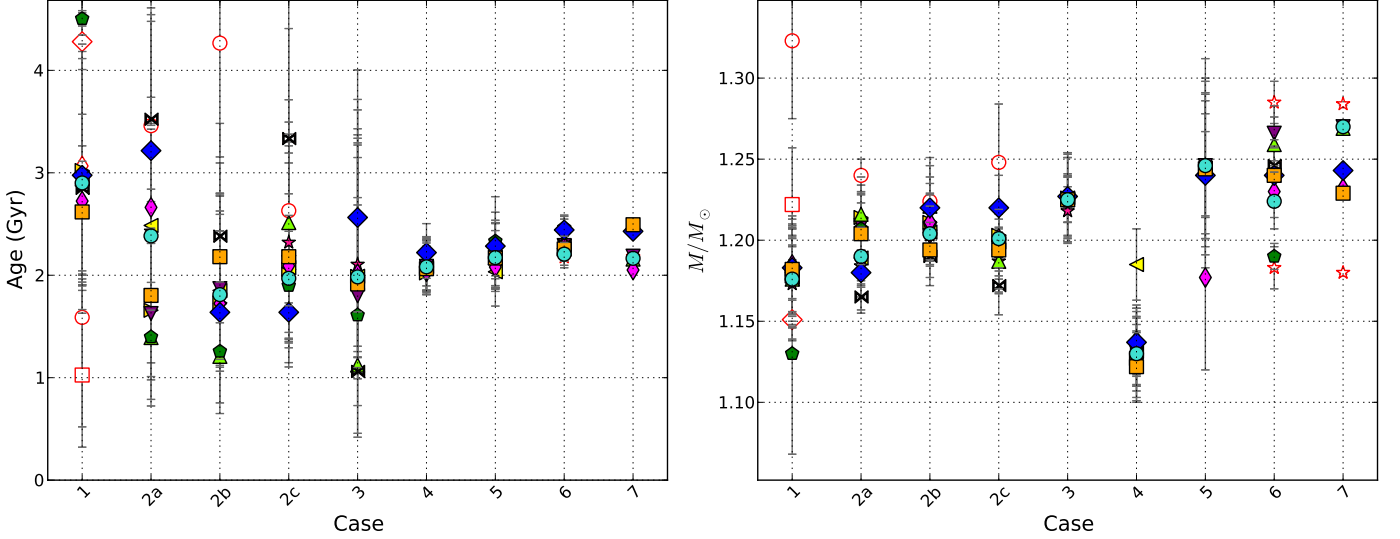


Fig. 4. The ranges of ages (left) and masses (right) derived from stellar model optimization for HD 52265. In abscissae, are listed the cases numbers, as defined in Table 3. For each case, several model optimizations can be identified according to the symbols and colours indicated in Table 2. In addition, open red symbols are for extra models of Set A described in Table A.1 of Appendix A.2: circles are for different, small Y_0 value, square and diamond are for small and high α_{conv} values respectively, small diamond for model with large core overshoot. Red stars illustrate the Y_0 - M degeneracy in Cases 6 and 7 but the inferred range would be the same for all cases.

initial helium Y_0 slightly changes in the optimization because $\Delta Y/\Delta Z$ is fixed but Z/X is adjusted in the optimization. Note that for given input physics and free parameters (Cases 2a, 2b, 2c for set A in Tables 4), the age is significantly modified depending on the way the mean large frequency separation is computed, the changes are correlated with changes in the inferred mixing length values. *The scatter in the inferred mixing length values, hence on the age is smaller when $\langle \Delta \nu \rangle$ is calculated explicitly (i.e. not from the scaling relation) using the stellar models (Cases 2b and 2c).*

In Cases 3, the age scatter is slightly reduced with respect to Cases 2a. As already pointed out in Lebreton (2013), this is due to the fact that the additional constraint on ν_{max} does not bring much more knowledge on the age of the star.

Cases 4, 5, 6, 7 all take into account seismic constraints directly sensitive to age, i.e. either the small frequency separation d_{02} , or the frequency separation ratios r_{02} , $rr_{01/10}$, or the individual frequencies. The spectacular consequence is a reduction of the age scatter as can be seen in Fig. 4.

For Case 4, considering the different possible options for the input physics of the stellar models, our criterion $\chi^2_{\text{R,seism}} \leq 2$ excludes the model without microscopic diffusion (model E4). Accordingly, the ages range between 2.02 ± 0.22 Gyr (model J4) and 2.22 ± 0.27 Gyr (model C4). This yields an age of 2.15 ± 0.35 Gyr, i.e. an age uncertainty of $\sim \pm 16$ per cents.

For Case 5, considering the different possible options for the input physics of the stellar models, two models (I5, J5) are excluded because their initial helium abundance Y_0 is found to be much smaller than the primordial value Y_p . Accordingly the ages range between 2.08 ± 0.25 Gyr (model D5) and 2.33 ± 0.40 Gyr (model E5). This yields an age of 2.28 ± 0.45 Gyr i.e. an age uncertainty of $\sim \pm 20$ per cents. It is possible to reduce further this scatter. Indeed helioseismology has shown that microscopic diffusion must be included in the case of the Sun. This must also be true for solar like-stars like HD 52265: its mass is only slightly larger than the solar one and it has an extended convective envelope. Excluding the model without diffusion then yields an age

in the range 2.08 ± 0.25 Gyr (model D5) - 2.28 ± 0.31 Gyr (model C6), that is, an age of 2.21 ± 0.38 Gyr, i.e. an age uncertainty of $\pm 17\%$. Hence the main cause of scatter on the high side of the age interval here is microscopic diffusion (model E5) followed by the solar mixture (model C5). The low side of the age interval comes from the change of nuclear reaction rates (model D5). *This shows that we start to reach the quality level of data which enables to test the microscopic physics in stars other than the Sun.*

For Case 6, considering the different possible options for the input physics of the stellar models, our criteria $\chi^2_{\text{R,classic}} \leq 1$ and $\chi^2_{\text{R,seism}} \leq 2$ exclude models I6, J6 and K6. Accordingly, the ages range between 2.21 ± 0.11 Gyr (model A6) and 2.46 ± 0.08 Gyr (model E6). This yields an age of 2.32 ± 0.22 Gyr, i.e. an age uncertainty $\sim \pm 9.5\%$. The main cause of scatter here is microscopic diffusion closely followed by the choice of the solar mixture: GN93 (model A6) versus AGSS09 (model C6). The range for the mixing length value is $[0.588, 0.606]$. This range is considerably narrower than the one usually taken a priori to compute stellar models. Compared to the values we obtained from a calibration of a solar model with the input physics of reference set A ($\alpha_{\text{conv,cgm},\odot} = 0.688 \pm 0.014$), the values obtained for HD 52265 are smaller than the solar one by 12 – 15 per cents. The results for the initial helium abundance will be discussed in Sect. 4.3 below. It is worth pointing out that the range of ages obtained in Case 6 is quite close to the one obtained in Case 5. This can be understood by the fact that, as shown in Fig. 1, the mean value of $\langle rr_{01/10} \rangle$ is already a good indicator of the evolutionary state, at least if the classical parameters are also usable to constrain the stellar mass and if the convective core is small. We therefore reach similar accuracy in Case 5 and 6, but the precision on the individual ages is better in Case 6 which is more constrained by the use of individual ratios. Furthermore, as discussed in Sect. 4.6, in Case 6, the individual values $rr_{01/10}$ provide additional information on the star, unrelated to age. Their oscillatory behaviour which is related to steep gradients of the

sound speed, is an invaluable asset to characterize the depth of the convective envelope and the thermal and chemical structure at its radiative-convective interface (Lebreton & Goupil 2012). However, HD 52265 is a case study, with a small convective core, and we can expect that larger convective cores whose size is crucial for the age-dating would be better characterized by individual ratios than by their mean values.

For Case 7, considering the different possible options for the input physics of the stellar models, our criterion $\chi^2_{R, \text{seism}} \leq 2$ excludes several models (*E7*, *I7*, *J7*, *K7*). Accordingly, the ages range between 2.05 ± 0.02 Gyr (model *D7*) and 2.49 ± 0.02 Gyr (model *B7*). This yields an age of 2.27 ± 0.24 Gyr, i.e. an age uncertainty $\sim \pm 9.5\%$. The upper boundary of the age interval is due to the choice of the MLT approach for the convective transport (model *B7*) closely followed by the choice of the solar mixture (model *C7*). The lower boundary is due to changes in the nuclear rates (model *D7*).

To summarize, the best precision and accuracy, in the context of present input physics, is therefore obtained in Cases 4 - constrained by the mean values of the large and small frequency separations, Cases 6 - constrained by the individual values of the frequency separation ratios, and Cases 7 - constrained by individual frequencies. However, as stressed above Cases 4 and 7 suffer from the caveat that the individual frequencies were corrected from surface effects. As can be seen from model A7-noSE in Appendix A, the age is increased by more than 40 per cent in a model optimized without correcting for these effects. We therefore consider that Case 6 is the optimal choice of observational constraints regarding the age of the star (see also the discussion by Silva Aguirre et al. 2013).

Extra models, based on different choices for the optimization (correction from surface effects, correlations between the seismic ratios, etc.), do not imply drastic changes in the optimized age (see Appendix A.2).

Age-mixing length degeneracy: Figure 5, left panel shows the relation between the convection parameter α_{conv} and age of the optimized models. There is a possible trend for α_{conv} to increase with age. From a linear regression we got $\alpha_{\text{conv}}/\alpha_{\text{conv}, \odot} \simeq 0.13 \times A + 0.59$ where the age is in Gyr. This trend can be understood as follows. Higher ages on the MS would imply lower T_{eff} and larger radii. The radius of a star is smaller for a more efficient convective energy transport. Smaller radii, hence higher α_{conv} -related to more efficient convection- are therefore needed to bring T_{eff} back into the observational range. However, we checked that the ages determined by model optimization in Cases 6 and 7 are not affected by this possible degeneracy because allowed variations of α_{conv} along the regression line are limited by the constraints on T_{eff} and $[\text{Fe}/\text{H}]$.

4.3. Mass and initial helium abundance

Figure 4, right panel shows for each case in Table 3, the mass of the optimal model for a given set of physics in Table 2. Like the age, the mass is better constrained when seismic data are taken into account, in particular when seismic constraints explicitly sensitive to mass are used (large frequency separation, frequency at maximum power as in Cases 2 and 3).

Optimization of models of Case 3 relies on the scaling-relations (Eqs. 4 and 6). These models have therefore the peculiarity that their mass and radius are tightly fixed because scaling relations provide quite precise values of the mass and radius. On the other hand, the accuracy of the derived values for the mass and radius depend on the accuracy of the scaling re-

lations. As proposed in Sect. 4.2, models of Case 6, optimized with the frequency separation ratios, provide the best age but since they do not constrain surface layers, they do not fix the mass explicitly. On the other hand, the ages of models of Case 7 are less secure because they are affected by the correction of surface effects. Nevertheless, as can be seen from model A7-noSE in Appendix A.2, correction of surface effects only slightly modifies the optimized mass. Thus, we suggest that models of Case 7, optimized with the individual frequencies, are probably more suitable for mass determination.

Mass-initial helium abundance degeneracy: Figure 5, right panel, shows the relation between the initial helium abundance Y_0 and mass M of the optimized models. Like in Baudin et al. (2012), a clear anti-correlation between Y_0 and M is found. The smaller Y_0 , the larger M . From a linear regression, we derived $Y_0 \simeq -0.58 \times M/M_{\odot} + 1.00$ with a scatter about this mean value of less than ± 0.02 .

This Y_0 - M degeneracy is in agreement with what is expected from homology relations (see e.g. Cox & Giuli 1968). For a MS star in the domain of mass of HD 52265, the luminosity varies as $L \propto \mu^{7.5} M^{5.5} R^{-0.5}$ with $R \propto \mu^{0.55} M^{0.73}$ (CNO cycle) or $R \propto \mu^{-0.43} M^{0.14}$ (pp chain). Also, for a fully ionized gas, $\mu \approx 4/(8 - 5Y - 6Z)$ which increases with Y . Therefore, for a given observed luminosity -fixed in the optimization process- there are a range of couples (Y_0, M) leading to the same L value. The Y_0 - M degeneracy may severely hamper the determination of the mass of HD 52265 as shown by the results of Cases 4 and 5. A large scatter in the mass value is obtained. However low mass models such as those found in Case 4 have high values of Y_0 (i.e. larger than 0.33) which are hardly acceptable. More reasonable Y_0 values (i.e. smaller than 0.30) would yield models with masses larger than $1.20 M_{\odot}$.

For Set A, Cases 6 and 7, we calculated extra optimized models with different (Y_0, M) couples. Results are given in Appendix A.2 and appear as open red stars in the different figures. For our preferred Case 7, taking into account the Y_0 - M degeneracy and keeping Y_0 in the range 0.26-0.32, we found reference models of Set A with masses in the range $1.18 - 1.28 M_{\odot}$ and $\Delta Y/\Delta Z$ in the range 0.4 - 2.3. The scatter in mass around the central value is of ~ 5 per cents. In addition, for a given model, changing the physics would induce a mass scatter of about $0.04 M_{\odot}$ (~ 3 per cents). We note that, as is found in solar modelling, models *C* optimized with the AGSS09 solar mixture show a trend towards lower Y_0 , related to their lower metallicity. Further impact of the Y_0 - M degeneracy will be discussed below.

4.4. Radius and surface gravity

Figure 3 (top, left) shows that the range of surface gravities of the models is very tight which means that $\log g$ is very well determined by the modelling and is hardly sensitive to the input physics (see also the determinations of the seismic surface gravities of Kepler stars by Mathur et al. 2012; Metcalfe et al. 2012). For HD 52265, taking into account the Y_0 - M degeneracy, seismic models of Cases 6 and 7 have $\log g$ in the range 4.28 - 4.32 which improves by a factor of ten the precision on $\log g$ with respect to spectroscopy. We point out that for this star, the central value of the spectroscopic $\log g$ (4.32 ± 0.20 dex) is in good agreement with both the value inferred from the scaling relation (4.29 ± 0.01 dex) and our seismic optimized value (4.30 ± 0.02). This would not be the case for all the stars. The potential of asteroseismology to improve the determination of surface gravity and therefore of spectroscopic parameters (T_{eff} , $[\text{Fe}/\text{H}]$) has already been demonstrated. For instance, it has been applied to

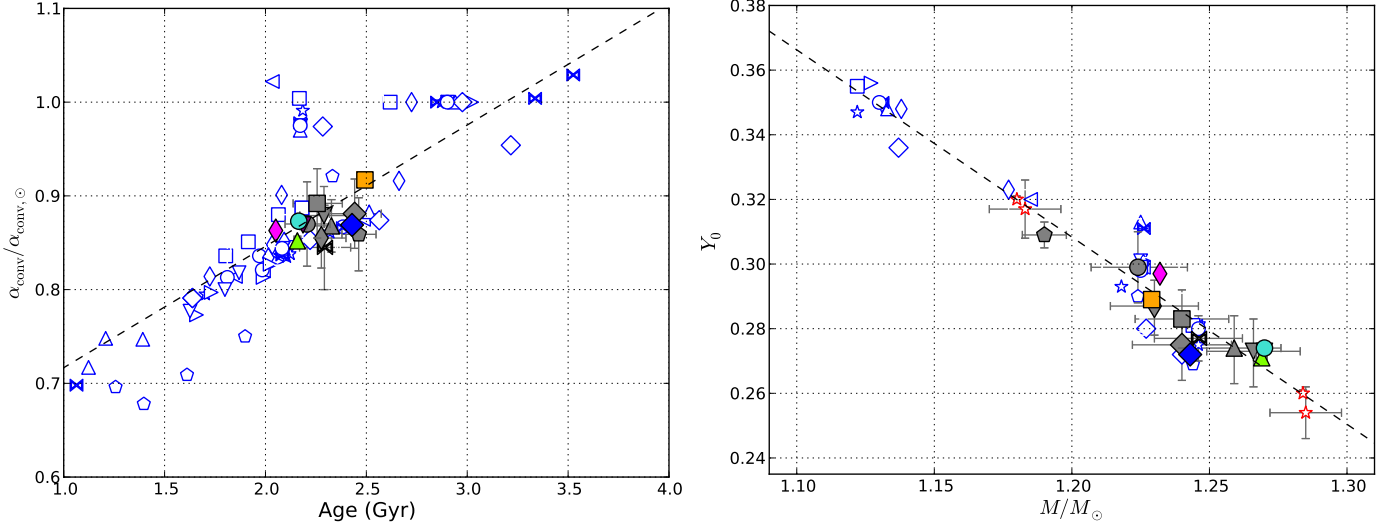


Fig. 5. Left: Relation between the convection parameter α_{conv} and the age. To compare models, we expressed α_{conv} in units of the solar value which, as mentioned in Sect. 3.1, mainly depends on the convection theory used in the model, i.e. $\alpha_{\text{conv},\odot,\text{cgm}} = 0.688$ and $\alpha_{\text{conv},\odot,\text{mlt}} = 1.762$. The regression line is $\alpha_{\text{conv}}/\alpha_{\text{conv},\odot} \approx 0.13 \times A + 0.59$ (A in Gyr.). Colour symbols are for Case 7 models (symbols and colours are listed in Tables 2), grey symbols for Case 6 and open blue for other cases. **Right:** Relation between the initial helium abundance and the mass of HD 52265, as inferred from model optimization. The regression line is $Y_0 \approx -0.58 \times M/M_\odot + 1.00$. Open red stars illustrate the impact of the Y_0 - M degeneracy (Table A.1).

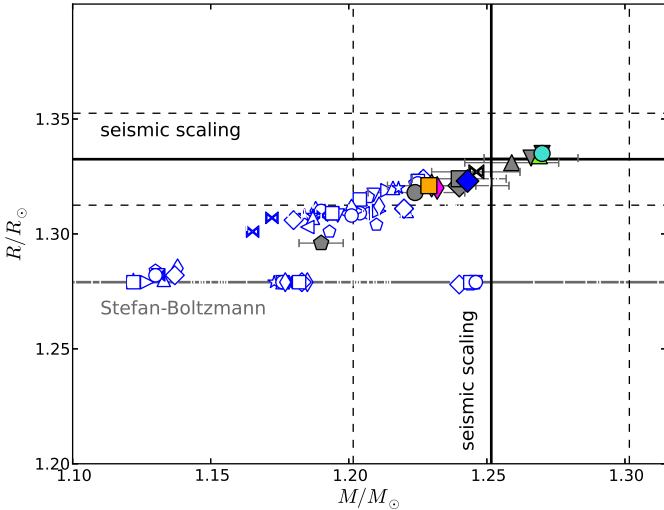


Fig. 6. Relation between the radius and the mass of HD 52265, as inferred from model optimization. Colours are for optimized models of Case 7 of Table 3 for different input physics, as listed in Table 2. Models for Case 6 are in grey, other cases are shown with open blue symbols. Bold solid horizontal and vertical black lines represent the values of the mass and radius derived from the scaling relations (Sect. 2.2.2). The corresponding uncertainties are displayed with dashed lines. The radius obtained using the Stefan-Boltzmann relation (Sect. 2.1) is shown in triple-dot dashed line. Three groups of models lie on the Stefan-Boltzmann line. There are Case 1, 4, and 5 models, discussed in the text.

the spectroscopic analysis of two CoRoT targets by Morel et al. (2013), and proposed for the calibration of $\log g$ of Gaia stars by Creevey et al. (2013).

The results for the star radius are shown in Fig. 6. Interestingly, all models have a radius in-between the Stefan-Boltzmann radius $R_{\text{SB}} = 1.28 \pm 0.06 R_\odot$ and the scaling ra-

dius $R_{\text{sc}} = 1.33 \pm 0.01 R_\odot$. Three groups of models lie on the Stefan-Boltzmann line. There are Case 1 models –which is expected because they were optimized with only the classical parameters– and nearly all models of Case 4 and 5. In the optimisation process, these latter are those that reproduce at best the observed effective temperature and luminosity of HD 52265. Case 6 and Case 7 models with different input physics and accounting for the Y_0 - M degeneracy, have seismic radii in the range $1.30 - 1.34 R_\odot$. This represents a precision of $\approx \pm 1.5$ per cent on the radius, that is a nice improvement with respect to what can be obtained with the Stefan-Boltzmann law ($\approx \pm 5$ per cents) for HD 52265.

4.5. Internal structure

HD 52265 has a very small convective core and a convective envelope. For instance, in model A7, the convective core has a mass $M_{\text{cc}} \sim 0.014 M_\star$ and a radius $R_{\text{cc}} \sim 0.045 R_\star$ while the radius at the basis of the convective envelope is of $R_{\text{zc}} \sim 0.80 R_\star$. These quantities can be quite different in other models which are nevertheless seismically equivalent. In particular, the Y_0 - M degeneracy has a major impact on the core mass. For instance changing Y_0 from 0.26 to 0.32 changes M_\star from 1.28 to $1.18 M_\odot$, M_{cc} from 0.006 to $0.023 M_\star$, and R_{cc} from 0.035 to $\sim 0.053 R_\star$. The depth of the convective envelope is unaffected.

Models optimized with rather high, currently accepted or predicted values of core overshooting (sets *I* and *J*), show quite high values of $\chi^2_{\text{R,seism}}$, indicating that overshooting is probably ruled out for this star. We investigated this point further by performing an optimization where we also adjusted the overshooting parameter (models A6-ov and A7-ov, in the Appendix). We found that quite low overshooting is indeed preferred, with α_{ov} in the range 0.0 – 0.04. In principle, seismology has the potential to discriminate between different values of overshooting even for small cores, through the signature left in the oscillation spectrum by the convective core (see the recent works by Silva Aguirre et al. 2013; Brandão et al. 2013, and references

therein). Such diagnostics are beyond the scope of the paper. However, we made some additional tests that indicate that, in the case of HD 52265, the seismic data are probably not precise enough to allow to infer the size of the mixed core precisely nor accurately.

4.6. Seismic properties

In Fig. 7, we show how the stellar models succeed -or not- in matching observed oscillation frequencies and frequency separations. Since a thorough examination of seismic properties of all the models is beyond the scope of this paper, we made a selection of models. The top left figure shows the échelle diagram corresponding to model of Case A7, optimized on the basis of the individual frequencies. When surface effects are corrected for, the model succeeds rather well in reproducing the échelle diagram for a value of the adjustable parameter $b_{SE} = 4.2$ (Eq. 12) compatible with the solar value obtained by Deheuvels & Michel (2011) with quasi similar input physics ($b_{SE,\odot} = 4.25$). On the other hand, in the high frequency range, non corrected models do not match observations. In this respect models A6 (frequencies not corrected, not plotted) and A7 (with uncorrected frequencies) give similar results. Furthermore, the top right figure shows that model A7 reproduces quite well the observed individual large frequency separations $\Delta\nu_\ell(n)$. The bottom left panel figure shows the comparison of the observed and model individual frequency separation ratios $rr_{01/10}(n)$. Model A7 reproduces rather well the mean slope of the variation of the ratios, but not the oscillatory behaviour. As shown by Lebreton & Goupil (2012), this behaviour in HD 52265 is reproduced in models including penetrative convection below the convective envelope, like model of set *K* which is similar to set *A* but with $\xi_{PC} = 1.3$. The figure also shows the effect of the $Y - M$ degeneracy on the diagram. The larger the helium abundance, the higher the $rr_{01/10}(n)$ ratios. However, with the present accuracy on the data, it is hard to discriminate the models with different (Y , M) values. Finally, we plotted a model of set *I*, that takes into account a moderate amount of core overshooting ($\alpha_{ov} = 0.15$). As already pointed out in Section 4.5 above, the overshooting amount cannot be very large since even a moderate amount of overshooting is ruled out by the present data. The right panel of the bottom figures shows the fit of the $r_{02}(n)$ ratios. In this case, regarding the precision on the data, it is difficult to discriminate the models.

5. Ages from other methods

We hereafter estimate the age of HD 52265 on the basis of other age-dating methods (empirical or H-R diagram inversion). We compare the resulting ages with the age inferred from “à la carte” stellar modelling.

5.1. Empirical ages

5.1.1. Activity

The chromospheric activity and age of solar-type dwarfs appear to be anti-correlated. Empirical relations allow to rely the CaII H & K emission index $R'_{HK} = L_{HK}/L_{bol}$ to age (see e.g. Mamajek & Hillenbrand 2008, for a recent calibration). For HD 52265, values of $\log R'_{HK}$ listed in the literature are in the range $[-5.02, -4.59]$. These small values indicate very low chromospheric activity. Using the Mamajek & Hillenbrand R'_{HK} -age relation, we derived an age of 4.0 ± 3.0 Gyr. Also the ages can be roughly estimated from the Mamajek & Hillenbrand relation

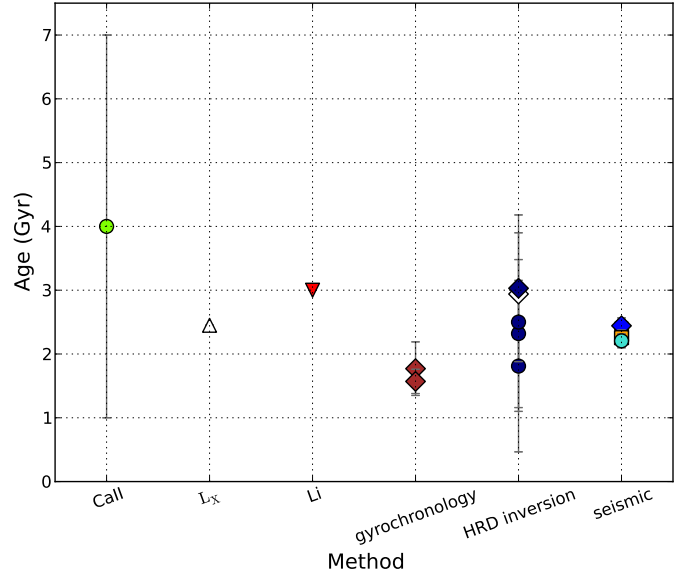


Fig. 8. Age estimates for HD 52265. Columns “CaII”, “ L_X ”, “Li” and “gyrochronology” give empirical estimates based on the R'_{HK} index (circle), lower limit from X-luminosity (upwards triangle), upper limit from lithium surface abundance (downwards triangle) and, gyrochronology (diamonds). Column “HRD inversion” shows estimates based on inversion of isochrones with circles for Padova isochrones and diamonds for BaSTI isochrones, full symbols for Bayesian methods, empty symbol for χ^2 -minimisation, see text. Column “seismic” shows the seismic determination for “à la carte” models of Cases 6 (Table 3 and Fig. 4)

between the fractional X-ray emission $R'_X = L_X/L_{bol}$ and age. For HD 52265, Kashyap et al. (2008) derived an upper limit, $L_X < 28.28$, which provides a lower age limit of 2.5 Gyr. Clearly, such empirical calibrations are too coarse to provide a reliable age of evolved stars with low chromospheric activity. Indeed, as recommended recently by Pace (2013), the use of chromospheric activity as a stellar clock should be limited to stars younger than about 1.5 Gyr.

5.1.2. Photospheric Lithium Abundance

At the surface of low mass stars, the lithium abundance can be depleted when the convective zone reaches the -not so deep- regions where Li is destroyed by nuclear reactions at $T \approx 2.5 \times 10^6$ K or, if mixing processes carry Li from the basis of the convective zone to the nuclear burning region. A relation between the Li-abundance, effective temperature and age is observed (but not fully understood). We used the Li abundance curves as a function of T_{eff} published by Sestito & Randich (2005) for clusters of different ages and derived a lower limit of 2.5 Gyr on the age of HD 52265 from several published values of its surface Li abundance ($\log \epsilon_{Li} \in [1.67, 2.88]$). With $\log \epsilon_{Li} = 2.40 \pm 0.06$ from Gonzalez et al. (2010), we found an age < 3 Gyr.

5.1.3. Gyrochronology

In the course of their evolution, solar-type stars lose angular momentum via magnetic braking due to their mass loss. It leads to a decrease of their rotation rate, first quantified by Skumanich (1972). Gyrochronology, as proposed by Barnes

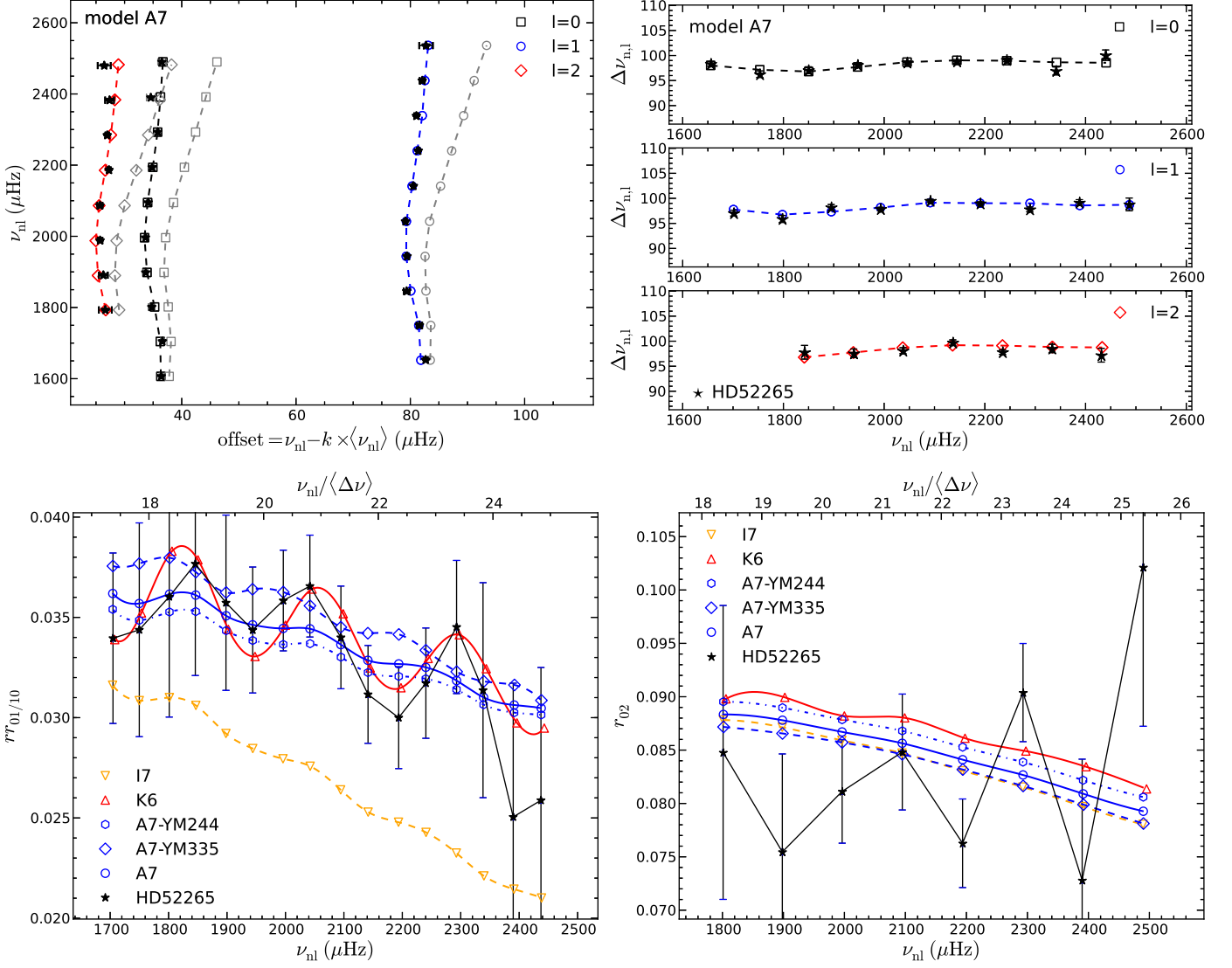


Fig. 7. Seismic properties of a selected set of models. *Top left panel:* Échelle diagram for the best model A7, optimized on the basis of the individual frequencies and including -or not- the correction of surface effects. “Star” symbols are for the observed frequencies while black squares, blue circles, and red diamonds are the model frequencies for angular degrees $\ell = 0, 1, 2$ respectively. In grey, are indicated the corresponding data before correction from surface effects. *Top right panel:* Comparison of observed large frequency separations for Case A7 (corrected frequencies). The symbols are the same as in the top right figure. *Bottom left panel:* Comparison of the observed frequency separation ratios $rr_{01/10}(n)$ for a selected set of models, including the best model A7 (continuous blue line). Results for models A7-YM-244 (pentagons) and A7-YM335 (diamonds) illustrate the effect of the Y-M degeneracy. Results for model K6 (continuous red line) show the effect of including penetrative convection below the convective envelope while results for model I7 (dashed orange line) show the effect of a moderate overshooting of the convective core. *Bottom right panel:* Same as in the bottom left figure but for the $r_{02}(n)$ frequency separation ratios.

(2007), is a new method to derive the age of solar-type stars via an empirical relation linking their rotation period, colour, and age, $t_{\text{Myr}}^n = P_{\text{days}} \times a^{-1} \times ((B - V) - c)^{-b}$ where a, b, c are constants. The constants were calibrated on the Sun, nearby field stars and clusters by Barnes (2007) and then revised by Mamajek & Hillenbrand (2008). We applied these relations to HD 52265 ($P_{\text{rot}} = 12.3 \pm 0.14$ days, see Sect. 2) and found an age of 1.57 ± 0.19 Gyr with Barnes’s values of a, b, c and 1.77 ± 0.42 Gyr with Mamajek & Hillenbrand values.

5.2. Age from pre-calculated sets of model isochrones

This method consists in placing a star in a H–R diagram and in interpreting its position by means of a grid of pre-calculated theoretical isochrones or evolutionary tracks. It is widely used to age-date large samples of stars, for galactic evolution studies (see e.g. Casagrande et al. 2011, and references therein). Different inversion techniques can be used to extract the stellar age (and mass) from theoretical isochrones. However, in several regions of the H–R diagram, for instance when the star is close to the zero age main sequence (ZAMS) or at turn-off, the morphology of the isochrones is complex leading to severe age degeneracy. To cope with these problems, Pont & Eyer (2004) and

Jørgensen & Lindegren (2005) proposed to take a Bayesian approach, with several priors, in particular one on the initial mass function.

Bayesian inversion techniques using the Padova isochrones give ages of 2.5 ± 1.4 Gyr (Holmberg et al. 2009) and 2.32 ± 1.16 Gyr (Casagrande et al. 2011). Also, we used the Girardi et al. (2002) and da Silva et al. (2006) PARAM web interface¹ and found an age of 2.81 ± 1.49 Gyr. On the other hand, from the use of BaSTI isochrones (Pietrinferni et al. 2004), Casagrande et al. obtained 3.03 ± 1.15 Gyr. Still with BaSTI isochrones, using the tools developed by Guédé et al. (2013), we inferred 2.94 Gyr from a χ^2 -minimisation. As can be seen in Fig. 8, the ages obtained cover a large range, 0.5–4.2 Gyr, due to the different isochrones grids and inversion methods used. For the star HD 52265 which is approximately half-way on its MS, we expect the isochrone inversion technique and the optimization performed in Case 1 of the present study to be equivalent in terms of precision -for a given set of input physics- because they are both based on the observational constraints on the classical parameters. However, the isochrone grid to be used for the inversion has to be dense enough both in mass and chemical composition. On the other hand, for stars lying in regions of degeneracy in the HR diagram, priors should be included in the optimization process in Case 1 in order to deal with multiple possible solutions (see e.g. Jørgensen & Lindegren 2005).

5.3. Comparison of ages from different methods

In Fig. 8, ages of HD 52265 obtained from different methods are compared. As discussed before, the ages from the R'_{HK} index, the X-luminosity, and the lithium surface abundance are not reliable for this star. The ages from gyrochronology are very precise but not accurate because gyrochronology is an empirical method that relies on calibrations (on the solar, nearby stars and cluster ages). As pointed out by D. Soderblom (2013, invited review talk at the International Francqui Symposium), seismic ages combined with precise rotation periods as provided by the Kepler or CoRoT missions, will give the potential to more fully test and calibrate the method of gyrochronology. Finally, there is a large scatter in the ages derived from H-R diagram inversion. This scatter is comparable to the one obtained in Cases 1 stellar modelling, when no seismic constraints are available. The “à la carte” seismic age-dating that we obtained in the present study, is by far the most precise.

6. Age and mass of the exoplanet orbiting HD 52265

A first estimate of the mass of the exoplanet orbiting HD 52265 was proposed by Butler et al. (2000) using their RV measurements and Eq. 1. From a grid of stellar models, Butler et al. inferred the mass of the star, first by placing the star in a colour-magnitude diagram at solar metallicity, and then, by correcting for the metallicity of the star –which they estimated to be $[\text{Fe}/\text{H}] = 0.11$, using stars of published mass and metallicity. They inferred a stellar mass of $1.13 \pm 0.03 M_{\odot}$ (note that the error bar here is an internal error bar and does not take into account the uncertainties of the stellar models) and deduced that the exoplanet has a mass $M_p \sin i = 1.13 M_{\text{Jupiter}}$. They did not give uncertainties on this determination, nor the values for the age of the host-star.

Using the RV data by Butler et al. (2000) and isochrone fits to derive the mass of the host-star, Gizon et al. (2013) es-

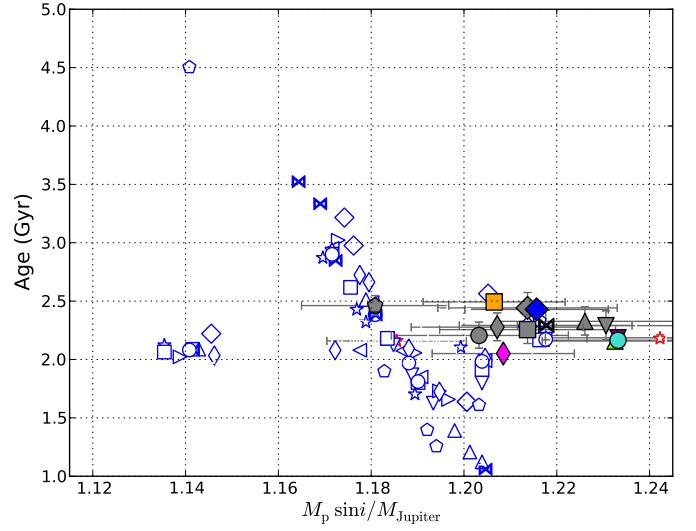


Fig. 9. Age and mass of the exoplanet $M_p \sin i$ inferred from the mass of its host-star. Colours are for optimized models of Case 7 of Table 3 for different input physics, as listed in Table 2. Models for Case 6 are in grey, other cases are shown with open blue symbols. The group of models with low mass and age of ~ 2 Gyr are Case 4 models, to be rejected because of their high initial helium abundance (see text).

timated the minimum mass of the exoplanet to be $M_{p,\text{min}} = 1.09 \pm 0.11 M_{\text{Jupiter}}$ (i.e. $\sin i = 1$ in Eq. 1). Here, again, the error bar does not account for the uncertainties of stellar models. Furthermore, with their measure of the inclination of the spin axis of the star ($\sin i = 0.59^{+0.18}_{-0.14}$, assumed to be also the axis of the planetary orbit), they estimated the mass of the exoplanet to be $M_p = 1.85^{+0.52}_{-0.42} M_{\text{Jupiter}}$. Note that the dominant source of error is the $\sin i$ error.

We have re-estimated the exoplanet mass, on the basis of the range of mass of the host-star here-before discussed. Figure 9 shows the range of mass of the exoplanet as a function of its age, supposed to be the age of the host-star, for the different physical options and optimization sets considered. When considering all cases, the scatter is quite large. In particular, models of Case 4, which correspond to low stellar mass, form the bunch of points at low planet mass, and at age around 2 Gyr but note that these models have to be excluded because of their very high initial helium abundance. On the other hand, the use of seismic constraints in Cases 6 and 7 considerably narrows the range of ages of the star while they mostly favour higher masses with respect to other cases (see Figs. 4). Hence, these optimized models, predict a higher mass for the exoplanet. Taking into account the $Y_0 - M$ degeneracy and excluding models E with no microscopic diffusion, the exoplanet mass $M_p \sin i$ is found to be in the range $1.16 - 1.26 M_{\text{Jupiter}}$ where we included the error budget due to the error on the host-star mass optimization and on the RV data characterizing the exoplanet orbit. The scatter around the central value is therefore $\sim \pm 4$ per cents. These values of the mass are higher (≈ 7 per cents) than the value of Butler et al. (2000). Furthermore, with the extreme values of $\sin i$ given by Gizon et al. (2013), the mass of the exoplanet would be in the range $1.5 - 2.8 M_{\text{Jupiter}}$. The scatter is a bit larger than the one in the result by Gizon et al. because we accounted for the uncertainties in the stellar models inputs. We therefore confirm that the companion of HD 52265 is a planet, not a brown dwarf.

¹ <http://stev.oapd.inaf.it/cgi-bin/param>

7. Conclusions

The optimization of models of the star HD 52265 using both classical and seismic observational data provides strong constraints on the age, mass, radius, and surface gravity of the star, and on the mass of its exoplanet. Taking into account the full information provided by seismic observations and considering the current uncertainties affecting the calculation of stellar models, we found an age $A = 2.10 - 2.54$ Gyr, a mass $M/M_{\odot} = 1.14 - 1.32$, a radius $R/R_{\odot} = 1.30 - 1.34$, and a surface gravity $\log g = 4.28 - 4.32$.

We stress that in the present case, the mass and radius given by the scaling relations agree quite well with the result of the full modelling. This can be explained by the fact that the effective temperature used in the scaling relations is accurately determined by spectroscopy and does correspond to the evolutionary stage of the star for its metallicity.

The mass of the exoplanet is found to be in the range $M_p \sin i = 1.16 - 1.26 M_{\text{Jupiter}}$. This represents considerable progress with respect to what can be achieved without seismic data or when using only mean values inferred from seismic observations, as the mean frequency separation and frequency at maximum power. An important point is that while the age, mass, radius of the star can be rather well-estimated from classical and mean seismic parameters once the input physics of the models are fixed, uncertainties on the input physics produce a large scatter of the results. We demonstrated here that taking full profit of seismic data -in particular considering the frequency separation ratios- considerably reduces this scatter by allowing to estimate free parameters of the models.

The full optimization performed here allowed us to better estimate the uncertainties and identify their origin, in particular concerning the age.

When no seismic constraints are available, the main cause for the age scatter and inaccuracy are the values of the mixing length and initial helium abundance belonging to a wide interval of possible values. Seismic constraints allowed to estimate such free parameters of stellar models, as the mixing-length parameter for convection and the core overshoot and penetrative convection parameters. As a result, the interval of possible values for α_{conv} , [0.59, 0.61], is considerably narrowed. These values are smaller by 12 – 15 per cents than the solar values obtained by a solar calibration using the same input physics. This provides an observational constraint on the convective transport efficiency which can be confronted with results of 3-D numerical simulations. The initial helium abundance could also be obtained but there remains a degeneracy between helium and mass. In order to remove this degeneracy, more precise oscillation frequencies are required. As studied by Houdek & Gough (2007), it would allow to detect an oscillatory behaviour of the frequencies resulting from changes in the adiabatic exponent in the second helium ionization zone, a seismic diagnostic of the helium abundance. Once the mixing length and initial helium abundance are unlocked, we find that the main cause of the age scatter is due to the choice of the solar mixture. *Once this issue is settled, we will then be at the level of testing nuclear reactions rates and internal transport processes, as demonstrated here.*

Presently, the availability of precise observational frequencies for close well-known stars only concerns a small number of stars among which very few host an exoplanet. These calibrators are precious to better understand the physics governing stellar interiors. A crucial need for the future is to increase the number of such calibrators. In this context, the ESA-PLATO high-precision photometry mission is really needed (Rauer et al. 2013). It will

provide essential information complementing the classical data that will be provided, with ultra high accuracy, by the Gaia-ESA mission, and interferometry and spectroscopic ground-based observations. Obtaining numerous and precise asteroseismic data is also a necessary step to make towards the full characterization of the age, mass, and radius of exoplanets. It is only with this effort that we will get a new understanding of the interiors, habitability and formation scenario of exoplanets and exoplanetary systems.

Acknowledgements. This research has made use of the SIMBAD database, operated at CDS, Strasbourg, France and of the NASA’s Astrophysics Data System. We warmly thank Kévin Belkacem for his comments on the manuscript.

References

- Anders, E. & Grevesse, N. 1989, *Geochim. Cosmochim. Acta*, 53, 197
 Angulo, C., Arnould, M., Rayet, M., et al. 1999, *Nuclear Physics A*, 656, 3
 Asplund, M., Grevesse, N., Sauval, A. J., & Scott, P. 2009, *ARA&A*, 47, 481
 Audard, N., & Provost, J. 1994, *A&A*, 282, 73
 Baglin, A., Auvergne, M., Barge, P., et al. 2002, in *ESA Special Publication*, Vol. 485, *Stellar Structure and Habitable Planet Finding*, ed. B. Battrick, F. Favata, I. W. Roxburgh, & D. Galadi, 17–24
 Baglin, A., Michel, E., & Noels, A. 2013, in *Astronomical Society of the Pacific Conference Series*, Vol. 479, *Astronomical Society of the Pacific Conference Series*, ed. H. Shibahashi & A. E. Lynas-Gray, 461
 Ballot, J., Gizon, L., Samadi, R., et al. 2011, *A&A*, 530, A97
 Barban, C., Beuret, M., Baudin, F., et al. 2013, *Journal of Physics Conference Series*, 440, 012031
 Barnes, S. A. 2007, *ApJ*, 669, 1167
 Baudin, F., Barban, C., Goupil, M. J., et al. 2012, *A&A*, 538, A73
 Belkacem, K., Goupil, M. J., Dupret, M. A., et al. 2011, *A&A*, 530, A142
 Belkacem, K., Samadi, R., Mosser, B., Goupil, M.-J., & Ludwig, H.-G. 2013, in *Astronomical Society of the Pacific Conference Series*, Vol. 479, *Astronomical Society of the Pacific Conference Series*, ed. H. Shibahashi & A. E. Lynas-Gray, 61
 Böhm-Vitense, E. 1958, *ZAp*, 46, 108
 Brandão, I. M., Cunha, M. S., & Christensen-Dalsgaard, J. 2013, *MNRAS*
 Brandão, I. M., Doğan, G., Christensen-Dalsgaard, J., et al. 2011, *A&A*, 527, A37
 Brown, T. M., Christensen-Dalsgaard, J., Weibel-Mihalas, B., & Gilliland, R. L. 1994, *ApJ*, 427, 1013
 Burgers, J. M. 1969, *Flow Equations for Composite Gases*
 Butler, R. P., Vogt, S. S., Marcy, G. W., et al. 2000, *ApJ*, 545, 504
 Canuto, V. M., Goldman, I., & Mazzitelli, I. 1996, *ApJ*, 473, 550+
 Casagrande, L., Schönrich, R., Asplund, M., et al. 2011, *A&A*, 530, A138
 Chaplin, W. J., Basu, S., Huber, D., et al. 2014, *ApJS*, 210, 1
 Chaplin, W. J. & Miglio, A. 2013, *ARA&A*, 51, 353
 Christensen-Dalsgaard, J. 1988, in *IAU Symposium*, Vol. 123, *Advances in Helio- and Asteroseismology*, ed. J. Christensen-Dalsgaard & S. Frandsen, 295
 Cox, J. & Giuli, R. 1968, *Principles of Stellar Structure*, vol I & II (Gordon & Breach, New-York)
 Creevey, O. L., Thévenin, F., Basu, S., et al. 2013, *MNRAS*, 431, 2419
 da Silva, L., Girardi, L., Pasquini, L., et al. 2006, *A&A*, 458, 609
 Deheuvels, S. & Michel, E. 2011, *A&A*, 535, A91
 Escobar, M. E., Théado, S., Vauclair, S., et al. 2012, *A&A*, 543, A96
 Ferguson, J. W., Alexander, D. R., Allard, F., et al. 2005, *ApJ*, 623, 585
 Formicola, A., Imbriani, G., Costantini, H., et al. 2004, *Physics Letters B*, 591, 61
 Freeman, K. C. 1993, in *Astronomical Society of the Pacific Conference Series*, Vol. 49, *Galaxy Evolution. The Milky Way Perspective*, ed. S. R. Majewski, 125
 Gilliland, R. L., Marcy, G. W., Rowe, J. F., et al. 2013, *ApJ*, 766, 40
 Gilliland, R. L., McCullough, P. R., Nelan, E. P., et al. 2011, *ApJ*, 726, 2
 Gilmore, G. 1999, *Baltic Astronomy*, 8, 203
 Girardi, L., Bertelli, G., Bressan, A., et al. 2002, *A&A*, 391, 195
 Gizon, L., Ballot, J., Michel, E., et al. 2013, *Proceedings of the National Academy of Science*, 110, 13267
 Gonzalez, G., Carlson, M. K., & Tobin, R. W. 2010, *MNRAS*, 403, 1368
 Gough, D. O. 1990, in *Lecture Notes in Physics*, Berlin Springer Verlag, Vol. 367, *Progress of Seismology of the Sun and Stars*, ed. Y. Osaki & H. Shibahashi, 283
 Grevesse, N. & Noels, A. 1993, in *Origin and Evolution of the Elements*, ed. N. Prantzos, E. Vangioni-Flam, & M. Casse, 15–25

Gruberbauer, M., Guenther, D. B., & Kallinger, T. 2012, *ApJ*, 749, 109

Guédé, C., Lebreton, Y., Babusiaux, C., Haywood, M., & Pelat, D. 2013, *A&A*, submitted

Havel, M., Guillot, T., Valencia, D., & Crida, A. 2011, *A&A*, 531, A3+

Hernandez, X., Gilmore, G., & Valls-Gabaud, D. 2000, *MNRAS*, 317, 831

Holmberg, J., Nordström, B., & Andersen, J. 2009, *A&A*, 501, 941

Houdek, G. & Gough, D. O. 2007, *MNRAS*, 375, 861

Iglesias, C. A. & Rogers, F. J. 1996, *ApJ*, 464, 943

Jørgensen, B. R. & Lindegren, L. 2005, *A&A*, 436, 127

Kashyap, V. L., Drake, J. J., & Saar, S. H. 2008, *ApJ*, 687, 1339

Kawaler, S. D. 1988, *ApJ*, 333, 236

Kjeldsen, H. & Bedding, T. R. 1995, *A&A*, 293, 87

Kjeldsen, H., Bedding, T. R., & Christensen-Dalsgaard, J. 2008, *ApJ*, 683, L175

Koch, D. G., Borucki, W. J., Basri, G., et al. 2010, *ApJ*, 713, L79

Kurucz, R. L. 1993, *VizieR Online Data Catalog*, 6039, 0

Lebreton, Y. 2012, in *Astronomical Society of the Pacific Conference Series*, Vol. 462, *Progress in Solar/Stellar Physics with Helio- and Asteroseismology*, ed. H. Shibahashi, M. Takata, & A. E. Lynas-Gray, 469

Lebreton, Y. 2013, in *EAS Publications Series*, Vol. 63, *EAS Publications Series*, 123–133

Lebreton, Y. & Goupil, M. J. 2012, *A&A*, 544, L13

Lebreton, Y., Michel, E., Goupil, M. J., Baglin, A., & Fernandes, J. 1995, in *IAU Symposium*, Vol. 166, *Astronomical and Astrophysical Objectives of Sub-Milliarcsecond Optical Astrometry*, ed. E. Hog & P. K. Seidelmann, 135

Lebreton, Y. & Montalbán, J. 2009, in *IAU Symposium*, Vol. 258, *IAU Symposium*, ed. E. E. Mamajek, D. R. Soderblom, & R. F. G. Wyse, 419–430

Lebreton, Y., Montalbán, J., Christensen-Dalsgaard, J., Roxburgh, I. W., & Weiss, A. 2008, *Ap&SS*, 316, 187

Liu, C., Bailer-Jones, C. A. L., Sordo, R., et al. 2012, *MNRAS*, 426, 2463

Ludwig, H.-G., Freytag, B., & Steffen, M. 1999, *A&A*, 346, 111

Mamajek, E. E. & Hillenbrand, L. A. 2008, *ApJ*, 687, 1264

Mamajek, E. E., Meyer, M. R., & Liebert, J. 2002, *AJ*, 124, 1670

Marques, J. P., Goupil, M. J., Lebreton, Y., et al. 2013, *A&A*, 549, A74

Mathur, S., Metcalfe, T. S., Woitaszek, M., et al. 2012, *ApJ*, 749, 152

Metcalfe, T. S., Chaplin, W. J., Appourchaux, T., et al. 2012, *ApJ*, 748, L10

Michaud, G. & Proffitt, C. R. 1993, in *Astronomical Society of the Pacific Conference Series*, Vol. 40, *IAU Colloq. 137: Inside the Stars*, ed. W. W. Weiss & A. Baglin, 246–259

Michel, E., Baglin, A., Auvergne, M., et al. 2008, *Science*, 322, 558

Miglio, A. & Montalbán, J. 2005, *A&A*, 441, 615

Morel, P. & Lebreton, Y. 2008, *Ap&SS*, 316, 61

Morel, P. & Thévenin, F. 2002, *A&A*, 390, 611

Morel, T., Rainer, M., Poretti, E., Barban, C., & Boumier, P. 2013, *A&A*, 552, A42

Mosser, B., Michel, E., Belkacem, K., et al. 2013, *A&A*, 550, A126

Oti Floranes, H., Christensen-Dalsgaard, J., & Thompson, M. J. 2005, *MNRAS*, 356, 671

Pace, G. 2013, *A&A*, 551, L8

Peimbert, M., Luridiana, V., & Peimbert, A. 2007, *ApJ*, 666, 636

Perryman, M. 2011, *The Exoplanet Handbook*

Pietrinferni, A., Cassisi, S., Salaris, M., & Castelli, F. 2004, *ApJ*, 612, 168

Pont, F. & Eyer, L. 2004, *MNRAS*, 351, 487

Press, W. H., Teukolsky, S. A., Vetterling, W. T., & Flannery, B. P. 2002, *Numerical recipes in C++ : the art of scientific computing*

Rauer, H., Catala, C., Aerts, C., et al. 2013, *ArXiv e-prints*

Rogers, F. J. & Nayfonov, A. 2002, *ApJ*, 576, 1064

Roxburgh, I. W. 1992, *A&A*, 266, 291

Roxburgh, I. W. & Vorontsov, S. V. 1994, *MNRAS*, 268, 880

Roxburgh, I. W. & Vorontsov, S. V. 2003, *A&A*, 411, 215

Roxburgh, I. W. & Vorontsov, S. V. 2013, *A&A*, 560, A2

Scuflaire, R., Montalbán, J., Théado, S., et al. 2008, *Ap&SS*, 316, 149

Sestito, P. & Randich, S. 2005, *A&A*, 442, 615

Silva Aguirre, V., Basu, S., Brandão, I. M., et al. 2013, *ApJ*, 769, 141

Skumanich, A. 1972, *ApJ*, 171, 565

Soderblom, D. R. 2010, *ARA&A*, 48, 581

Soriano, M., Vauclair, S., Vauclair, G., & Laymand, M. 2007, *A&A*, 471, 885

Tassoul, M. 1980, *ApJS*, 43, 469

Ulrich, R. K. 1986, *ApJ*, 306, L37

Valle, G., Dell’Omodarme, M., Prada Moroni, P. G., & Degl’Innocenti, S. 2014, *A&A*, 561, A125

van Leeuwen, F., ed. 2007, *Astrophysics and Space Science Library*, Vol. 350, *Hipparcos, the New Reduction of the Raw Data*

VandenBerg, D. A. & Clem, J. L. 2003, *AJ*, 126, 778

Watson, A. 1998, *Science*, 279, 981

Zahn, J.-P. 1991, *A&A*, 252, 179

Table A.1. Specifications of extra optimized models assuming different prescriptions for the modelling.

Set	Case	Particularities	Figure symbol
A	1-Y / 2-Y	$Y = 0.25 / 0.27$	open red circle
A	1- α 0.550	$\alpha_{\text{conv}} = 0.550$	open red square
A	1- α 0.826	$\alpha_{\text{conv}} = 0.826$	open red diamond
A	1-ov0.30	$\alpha_{\text{ov}} = 0.30$	open red pentagon
A	1, 2a, 7- ν rad		not plotted
A	5-allfreq	-	not plotted
A	6-nocorrel	-	not plotted
A	6-interR	-	not plotted
A	6, 7-ov	optimized overshoot	not plotted
A	6, 7-YM	$Y - M$ degeneracy	open red star
A	7-noSE	no SE corrections	not plotted
A	7-bSE4.9	solar SE corrections	not plotted
A	7-pms	-	not plotted
A	7-rot	rotation	not plotted

Appendix A: Models with different input physics or optimization details

A.1. Optimization of set A models with alternate prescriptions

In the following, we present other optimization models, all based on the reference physics of set A (Table 2). These models were optimized following Table 3, but with different approaches or choices of free parameters, as hereafter described and listed in Table A.1. The results of the models are listed in Tables A.2 and A.3.

1. Cases 1-Y / 2-Y

As explained in the main text, in Cases 1 and 2a, b, c, the initial helium content Y could not be adjusted due to the lack of observational constraints. Here we investigate the consequence of not deriving Y from the $\Delta Y / \Delta Z = 2$ enrichment law (as was done in Cases 1 and 2 of Table 3). We sought for a solution with the lowest possible initial helium content, never lower than the primordial abundance. These choices have an important impact on the results and are therefore discussed in the main text. It is worth to point out that in Case A1-Y, it was possible to find a solution with a primordial helium abundance. This is because no seismic constraints were used in this Case. On the other hand, in Cases A2a-Y, b-Y, and c-Y, due to the seismic constraints introduced, we had to increase the helium abundance above the primordial one to find a solution in agreement with both the seismic and the classical observational constraints (we found that models with low Y have either a too low temperature or a too high luminosity.)

2. Cases 1- α 0.550, 1- α 0.826

In Case 1, α_{conv} could not be adjusted due to the lack of observational constraints and, as often seen in papers, the solar value $\alpha_{\text{conv},\odot}$ was used. Here, we investigated the impact of other choices and we sought for a solution for acceptable, extreme values of α_{conv} . Numerical 2-D simulations of convection suggest that α_{conv} could differ by a few tenths dex from the solar value (see e.g. Ludwig et al. 1999). We investigated changes of α_{conv} of 20 per cents around the solar value which correspond to $\alpha_{\text{conv},\text{min}} = 0.550$ and $\alpha_{\text{conv},\text{max}} = 0.826$. These choices have an important impact on the results and are therefore discussed in the main text.

3. Cases 1-ov30

No overshooting was assumed in the reference models of Case 1. Here, to estimate its impact, we chose a rather large

value, i.e. $\alpha_{ov} = 0.30$. The impact on Case 1 results are discussed in the main text.

4. Cases 1, 2, 7- ν_{rad}

In these models, the impact of mixing resulting from the radiative diffusivity associated to the kinematic radiative viscosity, is investigated. Following Morel & Thévenin (2002), we added an extra mixing diffusion coefficient $d_{rad} = D_R \times \nu_{rad}$ with $D_R = 1$ which limits gravitational settling in the outer stellar layers of stars with thin convective envelopes. As can be seen in Tables A.2 and A.3, the impact is small and will not be further discussed.

5. Case 5-allfreq

In the list of frequencies extracted by Ballot et al. (2011), 31 frequencies were given among which 28 were flagged as secure. In this model, we considered the 31 values and found that the impact is small and that the results remain inside the uncertainty range we gave in the main text.

6. Case 6-YM, 7-YM

For each optimization case, there are a range of initial helium-mass doublets (Y_0 , M) that provide seismically equivalent optimized models. We investigated the $Y_0 - M$ degeneracy by searching for optimized models with different values of Y_0 and M . As discussed in the main text, the impact on age is small but a range of possible masses of HD 52265 is found.

7. Case 6-nocorrel

As explained in the main text, in Case 6, we took into account the correlations between the frequency separation ratios and calculated the χ^2 from Eq. 13. In this model the correlations are not considered and the χ^2 is evaluated from Eq. 14. The impact is small and will not be further discussed.

8. Case 6-interr

Roxburgh & Vorontsov (2013) recently claimed that model fitting by searching for a best fit of observed and model separation ratios at the same radial orders n is incorrect, and that a correct procedure is to compare the model ratios interpolated to the observed frequencies. We followed this recommendation here. The impact is small and the results remain in the uncertainty range we gave in the main text.

9. Case 7-rot

As explained in the main text, rotation and its effects on the transport of angular momentum and chemicals is treated as in Marques et al. (2013) and we tuned the K_w coefficient entering the treatment of magnetic braking by winds in order to match the observed rotation period. The impact on age and mass is small for this rather evolved star. A thorough study of the effects of rotation on HD 52265 will be presented in a forthcoming paper.

10. Case 7-noSE and Case 7-bSE4.9.

As explained in the main text, in Case 7, we corrected the individual frequencies from the surface effects with the Kjeldsen et al. (2008) empirical prescription and we calibrated the b_{SE} parameter in Eq. 12 to get the best match between observed and modelled frequencies. In model 7-bSE4.9, we used the solar value of b_{SE} calibrated by Kjeldsen et al. (2008) and found that the impact on the results is small. In model 7-noSE, we did not correct frequencies from the surface effects. The impact is important, in particular on age. This is discussed in the main text.

11. Case 7-pms.

Main models have been calculated, starting the computation at the zero age main sequence. This model was evolved from the pre main sequence. The impact is small.

12. Cases 6 and 7-ov.

In models presented in the main text, overshooting was either neglected (sets $A - H$, K) or fixed (sets I , J). Since in Cases 6 and 7, there are enough observational constraints to add overshooting and penetrative convection as additional free parameters, we considered this possibility here. We therefore also optimized the values of α_{ov} and ξ_{PC} . As also discussed in the main text, we found that small values of α_{ov} are favoured (range 0.00 – 0.04) and rather high values of ξ_{PC} (range 0.90 – 1.25). This latter result, related to the oscillatory behaviour of the frequencies, close to the convective envelope is in agreement with the conclusions of Lebreton & Goupil (2012).

A.2. Optimization with different input physics

In the following, we present optimization models, based on the different choices of input physics listed in Table 2. These models were optimized following Table 3. The results are listed in Tables A.4 and A.5. Discussions are to be found in the main text.

Table A.2. Same as Table 4 but for different optimization options (see Sect. 3 and Tables A.1 and 3).

Model	Age (Gyr)	M/M_{\odot}	$(Z/X)_0$	Y_0	α_{mlt}	$\alpha_{\text{ov}} / \xi_{\text{PC}}$	b_{SE}	$a_{\text{SE}}/r_{\text{SE}}$	$\chi^2_{\text{R,classic}} / \chi^2_{\text{R,seism}}$
A1-Y	1.59± 2.17	1.32± 0.05	0.0447±0.0051	0.245	0.688	0.00/0.00	–	–	1.0 10 ⁻¹⁹ / –
A1-a10.550	1.03± 1.47	1.22± 0.03	0.0467±0.0066	0.309	0.550	0.00/0.00	–	–	1.4 10 ⁻¹³ / –
A1-a10.826	4.28± 0.78	1.15± 0.01	0.0471±0.0049	0.310	0.826	0.00/0.00	–	–	4.1 10 ⁻⁵ / –
A1-ov0.3	3.07± 1.35	1.18± 0.03	0.0487±0.0054	0.312	0.688	0.30/0.00	–	–	1.8 10 ⁻¹⁷ / –
A1-Renu	2.91± 1.30	1.18± 0.04	0.0481±0.0052	0.311	0.688	0.00/0.00	–	–	9.7 10 ⁻⁶ / –
A2a-Renu	2.21± 0.87	1.19± 0.02	0.0488±0.0051	0.312	0.580±0.096	0.00/0.00	–	–	1.5 10 ⁻¹ /5.9 10 ⁻⁴
A2a-Y	3.46± 0.95	1.24± 0.01	0.0472±0.0040	0.270	0.682±0.130	0.00/0.00	–	–	3.3 10 ⁻¹ /1.8 10 ⁻⁴
A2b-Y	4.27± 1.32	1.22± 0.03	0.0465±0.0047	0.270	0.744±0.148	0.00/0.00	5.5	-1.3/1.00	3.6 10 ⁻¹ /1.3 10 ⁻⁴
A2c-Y	2.63± 1.68	1.25± 0.04	0.0447±0.0046	0.270	0.604±0.060	0.00/0.00	5.5	-3.3/1.00	5.3 10 ⁻¹ /2.3 10 ⁻¹
A5-allfreq	2.25± 0.30	1.27± 0.04	0.0461±0.0056	0.265±0.030	0.698±0.081	0.00/0.00	–	–	8.7 10 ⁻⁷ /3.3 10 ⁻³
A6-YM254	2.45± 0.13	1.29± 0.01	0.0451±0.0027	0.254±0.008	0.683±0.032	0.00/0.00	–	–	7.3 10 ⁻² /8.1 10 ⁻¹
A6-YM317	2.18± 0.11	1.18± 0.01	0.0489±0.0025	0.317±0.009	0.591±0.026	0.00/0.00	–	–	6.7 10 ⁻² /8.9 10 ⁻¹
A6-intrr	2.20± 0.11	1.17± 0.03	0.0494±0.0033	0.324±0.017	0.603±0.031	0.00/0.00	–	–	1.9 10 ⁻² /8.6 10 ⁻¹
A6-nocorrel	2.28± 0.21	1.21± 0.04	0.0497±0.0051	0.302±0.024	0.595±0.052	0.00/0.00	–	–	1.8 10 ⁻¹ /7.2 10 ⁻¹
A6-ov	2.32± 0.14	1.25± 0.01	0.0481±0.0021	0.277±0.006	0.687±0.027	0.04/0.90	–	–	2.0 10 ⁻¹ /7.8 10 ⁻¹
A7-bSE4.9	2.18± 0.03	1.27± 0.00	0.0487±0.0006	0.274±0.001	0.601±0.004	0.00/0.00	4.9	-4.1/1.00	5.3 10 ⁻¹ /1.8 10 ⁰
A7-Renu	2.18± 0.02	1.27± 0.00	0.0489±0.0007	0.274±0.001	0.599±0.004	0.00/0.00	4.5	-4.7/1.00	4.9 10 ⁻¹ /1.7 10 ⁰
A7-YM-noSE	2.98± 0.03	1.24± 0.00	0.0628±0.0007	0.306±0.001	0.725±0.005	0.00/0.00	–	–	3.3 10 ⁰ /6.8 10 ⁰
A7-ov	1.93± 0.01	1.23± 0.00	0.0481±0.0007	0.291±0.001	0.564±0.003	0.00/1.25	3.6	-7.7/1.00	7.8 10 ⁻¹ /2.2 10 ⁰
A7-YM-ov	2.15± 0.03	1.23± 0.00	0.0485±0.0007	0.289±0.001	0.581±0.003	0.00/0.99	4.1	-5.9/1.00	5.7 10 ⁻¹ /1.8 10 ⁰
A7-noSE	3.14± 0.03	1.30± 0.00	0.0690±0.0008	0.276±0.001	0.731±0.005	0.00/0.00	–	–	4.7 10 ⁰ /4.0 10 ⁰
A7-pms	2.18± 0.02	1.27± 0.00	0.0486±0.0006	0.274±0.001	0.601±0.004	0.00/0.00	3.8	-6.2/1.00	5.2 10 ⁻¹ /1.7 10 ⁰
A7-YM244	2.14± 0.02	1.32± 0.00	0.0460±0.0008	0.244±0.001	0.588±0.004	0.00/0.00	4.5	-4.4/1.00	7.7 10 ⁻¹ /1.6 10 ⁰
A7-YM260	2.18± 0.03	1.28± 0.00	0.0467±0.0006	0.260±0.001	0.583±0.004	0.00/0.00	3.7	-6.4/1.00	5.9 10 ⁻¹ /1.6 10 ⁰
A7-YM300	2.14± 0.01	1.21± 0.00	0.0478±0.0006	0.300±0.001	0.585±0.004	0.00/0.00	3.8	-7.3/1.00	1.7 10 ⁻¹ /1.8 10 ⁰
A7-YM310	2.16± 0.02	1.20± 0.00	0.0484±0.0004	0.310±0.001	0.584±0.004	0.00/0.00	3.5	-8.2/1.00	1.2 10 ⁻¹ /1.9 10 ⁰
A7-YM320	2.17± 0.02	1.18± 0.00	0.0501±0.0004	0.320±0.001	0.585±0.004	0.00/0.00	3.5	-8.3/1.00	1.3 10 ⁻¹ /2.0 10 ⁰
A7-YM335	2.15± 0.02	1.15± 0.00	0.0491±0.0003	0.335±0.001	0.585±0.004	0.00/0.00	3.5	-2.0/1.00	2.6 10 ⁻² /2.1 10 ⁰
A7-rot	2.19± 0.03	1.27± 0.00	0.0488±0.0004	0.275±0.001	0.595±0.004	0.00/0.00	5.5	-3.3/1.00	1.3 10 ⁰ /2.6 10 ⁰

Table A.3. Same as Table 5 but for different optimization options (see Sect. 3 and Tables A.1 and 3)

Model	T_{eff} [K]	L [L_{\odot}]	[Fe/H] [dex]	$\log g$ [dex]	R [R_{\odot}]	$\langle \Delta \nu \rangle$ [μHz]	ν_{max} [μHz]	$\langle r_{02} \rangle$ –	$\langle rr_{01/10} \rangle$ –	X_C –	$\frac{\Delta Y}{\Delta Z}$ –	M_{cc} [M_{\star}]	R_{zc} [R_{\star}]	$M_p \sin i$ [M_{Jupiter}]
A1-Y	6116.	2.053	0.22	4.35	1.28	107.45	2393.	0.091	0.033	0.49	0.0	0.002	0.788	1.27±0.04
A1-a10.550	6116.	2.053	0.22	4.31	1.28	101.88	2210.	0.097	0.035	0.51	2.0	0.016	0.836	1.20±0.04
A1-a10.826	6116.	2.053	0.22	4.29	1.28	101.09	2081.	0.053	0.030	0.16	2.0	0.047	0.713	1.15±0.03
A1-ov0.3	6116.	2.053	0.22	4.30	1.28	101.27	2131.	0.072	0.011	0.43	2.0	0.140	0.769	1.17±0.04
A1-Renu	6116.	2.054	0.22	4.29	1.28	101.29	2125.	0.074	0.033	0.28	2.0	0.029	0.769	1.17±0.04
A2a-Renu	6046.	2.062	0.22	4.28	1.31	98.13	2064.	0.083	0.035	0.35	2.0	0.023	0.806	1.18±0.03
A2a-Y	6012.	2.069	0.21	4.28	1.33	98.13	2096.	0.070	0.033	0.27	0.7	0.024	0.759	1.21±0.03
A2b-Y	6008.	2.070	0.21	4.28	1.33	98.13	2063.	0.060	0.032	0.21	0.7	0.036	0.731	1.20±0.04
A2c-Y	6001.	2.060	0.19	4.29	1.33	98.26	2106.	0.080	0.034	0.33	0.7	0.010	0.791	1.22±0.04
A5-allfreq	6116.	2.053	0.22	4.33	1.28	105.37	2299.	0.083	0.033	0.39	0.5	0.007	0.778	1.23±0.04
A6-YM254	6074.	2.058	0.21	4.32	1.30	103.67	2263.	0.081	0.032	0.37	0.2	0.005	0.777	1.24±0.03
A6-YM317	6068.	2.048	0.22	4.28	1.30	98.69	2087.	0.084	0.034	0.35	2.2	0.022	0.804	1.18±0.03
A6-intrr	6094.	2.060	0.22	4.29	1.29	99.07	2085.	0.083	0.034	0.34	2.4	0.026	0.802	1.17±0.04
A6-nocorrel	6037.	2.054	0.23	4.28	1.31	98.29	2092.	0.083	0.034	0.35	1.7	0.020	0.799	1.19±0.04
A6-ov	6094.	2.039	0.26	4.32	1.28	104.20	2252.	0.082	0.032	0.39	0.9	0.017	0.729	1.22±0.03
A7-bSE4.9	6019.	2.101	0.23	4.29	1.34	98.29	2123.	0.084	0.034	0.39	0.8	0.014	0.800	1.23±0.03
A7-Renu	6013.	2.092	0.23	4.29	1.34	98.29	2125.	0.084	0.034	0.39	0.8	0.013	0.800	1.23±0.03
A7-YM-noSE	6069.	2.156	0.34	4.28	1.33	98.30	2076.	0.070	0.030	0.29	1.4	0.046	0.754	1.21±0.03
A7-ov	5989.	2.012	0.25	4.29	1.32	98.28	2112.	0.087	0.034	0.41	1.3	0.012	0.753	1.21±0.03
A7-YM-ov	5997.	2.030	0.25	4.29	1.32	98.28	2107.	0.085	0.034	0.38	1.3	0.013	0.756	1.21±0.03
A7-noSE	5983.	2.114	0.39	4.29	1.36	98.33	2122.	0.070	0.030	0.31	0.6	0.041	0.745	1.26±0.03
A7-pms	6021.	2.101	0.23	4.29	1.33	98.29	2125.	0.084	0.034	0.39	0.8	0.013	0.800	1.23±0.03
A7-YM244	5958.	2.073	0.21	4.30	1.35	98.29	2160.	0.086	0.033	0.42	0.0	0.003	0.800	1.27±0.03
A7-YM260	5971.	2.048	0.21	4.29	1.34	98.28	2141.	0.085	0.033	0.40	0.4	0.006	0.801	1.24±0.03
A7-YM300	6047.	2.067	0.21	4.29	1.31	98.28	2096.	0.084	0.034	0.37	1.7	0.017	0.806	1.20±0.03
A7-YM310	6047.	2.046	0.21	4.28	1.31	98.28	2087.	0.084	0.034	0.36	2.0	0.019	0.805	1.19±0.03
A7-YM320	6055.	2.038	0.23	4.28	1.30	98.28	2077.	0.084	0.034	0.35	2.3	0.023	0.804	1.17±0.03
A7-YM335	6090.	2.045	0.21	4.28	1.29	98.29	2058.	0.083	0.035	0.34	2.9	0.027	0.807	1.15±0.03
A7-rot	6034.	2.124	0.28	4.29	1.34	98.32	2121.	0.085	0.034	0.40	0.8	0.014	0.806	1.23±0.03

Table A.4. Same as Table 4 but for different input physics of the models (see Sect. 3 and Tables 2 and 3).

Model	Age (Gyr)	M/M_{\odot}	$(Z/X)_0$	Y_0	α_{mlt}	$\alpha_{\text{ov}} / \xi_{\text{PC}}$	b_{SE}	$a_{\text{SE}}/r_{\text{SE}}$	$\chi^2_{\text{R,classic}} / \chi^2_{\text{R,seism}}$
B1	2.62± 1.22	1.18± 0.03	0.0483±0.0053	0.311	1.762	0.00/0.00	–	–	4.6 10 ⁻⁷ / –
B2a	1.80± 0.85	1.20± 0.02	0.0493±0.0054	0.312	1.473±0.222	0.00/0.00	–	–	1.8 10 ⁻¹ /6.2 10 ⁻⁴
B2b	2.18± 0.78	1.19± 0.02	0.0491±0.0051	0.312	1.562±0.252	0.00/0.00	5.5	-4.8/1.00	1.2 10 ⁻¹ /1.9 10 ⁻⁴
B2c	2.18± 0.55	1.19± 0.01	0.0491±0.0051	0.312	1.562±0.242	0.00/0.00	5.5	-4.8/1.00	2.2 10 ⁻¹ /7.9 10 ⁻⁶
B3	1.91± 1.12	1.23± 0.01	0.0489±0.0053	0.299±0.019	1.500±0.241	0.00/0.00	–	–	2.6 10 ⁻¹ /1.7 10 ⁻²
B4	2.06± 0.24	1.12± 0.02	0.0511±0.0047	0.355±0.017	1.549±0.096	0.00/0.00	5.5	-5.4/1.00	3.2 10 ⁻⁵ /7.0 10 ⁻⁷
B5	2.17± 0.32	1.24± 0.05	0.0467±0.0061	0.281±0.040	1.769±0.229	0.00/0.00	–	–	7.4 10 ⁻⁷ /4.0 10 ⁻³
B6	2.26± 0.12	1.24± 0.02	0.0470±0.0020	0.283±0.009	1.571±0.065	0.00/0.00	–	–	3.0 10 ⁻¹ /8.3 10 ⁻¹
B7	2.49± 0.02	1.23± 0.00	0.0494±0.0005	0.289±0.001	1.615±0.009	0.00/0.00	3.5	-8.3/1.00	3.2 10 ⁻¹ /1.8 10 ⁰
C1	2.98± 1.33	1.18± 0.03	0.0358±0.0038	0.296	0.688	0.00/0.00	–	–	1.1 10 ⁻⁸ / –
C2a	3.22± 1.08	1.18± 0.02	0.0363±0.0037	0.297	0.656±0.111	0.00/0.00	–	–	1.0 10 ⁻¹ /9.8 10 ⁻⁵
C2b	1.64± 0.67	1.22± 0.02	0.0363±0.0053	0.297	0.544±0.074	0.00/0.00	5.5	-5.0/1.00	1.4 10 ⁻¹ /6.2 10 ⁻⁴
C2c	1.64± 0.66	1.22± 0.02	0.0363±0.0047	0.297	0.544±0.083	0.00/0.00	5.5	-5.0/1.00	1.5 10 ⁻¹ /3.6 10 ⁻⁴
C3	2.56± 1.18	1.23± 0.03	0.0361±0.0038	0.280±0.023	0.601±0.092	0.00/0.00	–	–	2.7 10 ⁻¹ /8.8 10 ⁻³
C4	2.22± 0.27	1.14± 0.02	0.0380±0.0032	0.336±0.016	0.587±0.048	0.00/0.00	5.5	-4.9/1.00	1.9 10 ⁻³ /2.5 10 ⁻⁶
C5	2.28± 0.31	1.24± 0.03	0.0346±0.0038	0.272±0.019	0.670±0.075	0.00/0.00	–	–	8.1 10 ⁻⁵ /2.5 10 ⁻³
C6	2.44± 0.13	1.24± 0.02	0.0363±0.0016	0.275±0.011	0.606±0.025	0.00/0.00	–	–	2.4 10 ⁻¹ /8.3 10 ⁻¹
C7	2.43± 0.03	1.24± 0.00	0.0358±0.0004	0.272±0.001	0.598±0.004	0.00/0.00	3.5	-7.6/1.00	2.9 10 ⁻¹ /1.5 10 ⁰
D1	2.72± 1.08	1.18± 0.02	0.0478±0.0055	0.310	0.688	0.00/0.00	–	–	8.2 10 ⁻⁷ / –
D2a	2.66± 0.90	1.19± 0.02	0.0485±0.0051	0.311	0.630±0.104	0.00/0.00	–	–	1.3 10 ⁻¹ /2.1 10 ⁻⁶
D2b	1.72± 0.87	1.21± 0.02	0.0492±0.0050	0.312	0.560±0.114	0.00/0.00	5.5	-4.4/1.00	1.5 10 ⁻¹ /1.4 10 ⁻³
D2c	2.09± 1.02	1.20± 0.02	0.0488±0.0052	0.312	0.585±0.093	0.00/0.00	5.5	-3.9/1.00	2.4 10 ⁻¹ /5.0 10 ⁻⁴
D3	2.01± 1.08	1.23± 0.03	0.0487±0.0068	0.300±0.026	0.574±0.083	0.00/0.00	–	–	2.6 10 ⁻¹ /1.6 10 ⁻²
D4	2.03± 0.24	1.14± 0.02	0.0501±0.0049	0.348±0.017	0.583±0.040	0.00/0.00	5.5	-4.4/1.00	5.6 10 ⁻³ /6.2 10 ⁻⁶
D5	2.08± 0.25	1.18± 0.06	0.0484±0.0050	0.323±0.045	0.620±0.159	0.00/0.00	–	–	4.2 10 ⁻⁵ /7.6 10 ⁻³
D6	2.28± 0.12	1.23± 0.02	0.0452±0.0017	0.287±0.008	0.588±0.022	0.00/0.00	–	–	3.9 10 ⁻¹ /8.1 10 ⁻¹
D7	2.05± 0.02	1.23± 0.00	0.0485±0.0007	0.297±0.001	0.594±0.004	0.00/0.00	4.3	-5.3/1.00	3.0 10 ⁻¹ /2.0 10 ⁰
E1	4.50± 1.70	1.13± 0.06	0.0405±0.0046	0.302	0.688	0.00/0.00	–	–	5.6 10 ⁻³ / –
E2a	1.40± 0.99	1.21± 0.02	0.0404±0.0046	0.302	0.466±0.082	0.00/0.00	–	–	1.9 10 ⁻¹ /3.9 10 ⁻⁴
E2b	1.26± 0.89	1.21± 0.02	0.0405±0.0046	0.302	0.479±0.085	0.00/0.00	5.5	-5.7/1.00	8.8 10 ⁻² /6.1 10 ⁻⁴
E2c	1.90± 1.06	1.19± 0.02	0.0406±0.0046	0.302	0.516±0.072	0.00/0.00	5.5	-5.1/1.00	1.8 10 ⁻¹ /2.2 10 ⁻³
E3	1.61± 1.44	1.22± 0.03	0.0406±0.0046	0.290±0.025	0.488±0.093	0.00/0.00	–	–	2.6 10 ⁻¹ /2.5 10 ⁻²
E4	1.79± 0.28	1.22± 0.02	0.0416±0.0047	0.291±0.018	0.515±0.034	0.00/0.00	5.5	-4.9/1.00	1.7 10 ⁻¹ /2.2 10 ⁰
E5	2.33± 0.40	1.24± 0.04	0.0406±0.0047	0.269±0.023	0.633±0.093	0.00/0.00	–	–	2.0 10 ⁻⁵ /3.3 10 ⁻³
E6	2.46± 0.08	1.19± 0.01	0.0462±0.0018	0.309±0.004	0.591±0.027	0.00/0.00	–	–	5.8 10 ⁻¹ /9.4 10 ⁻¹
E7	1.70± 0.01	1.23± 0.00	0.0417±0.0007	0.287±0.001	0.506±0.003	0.00/0.00	3.8	-9.0/1.00	4.3 10 ⁻¹ /7.1 10 ⁰
F1	2.85± 1.18	1.18± 0.02	0.0482±0.0052	0.311	2.000	0.00/0.00	–	–	1.5 10 ⁻⁶ / –
F2a	3.52± 0.96	1.17± 0.01	0.0482±0.0052	0.311	2.057±0.472	0.00/0.00	–	–	6.7 10 ⁻² /1.2 10 ⁻²
F2b	2.38± 0.93	1.19± 0.02	0.0491±0.0050	0.312	1.732±0.342	0.00/0.00	5.5	-4.1/1.00	1.2 10 ⁻¹ /6.7 10 ⁻²
F2c	3.33± 0.91	1.17± 0.02	0.0488±0.0050	0.312	2.008±0.331	0.00/0.00	5.5	-2.7/1.00	2.0 10 ⁻¹ /1.1 10 ⁻⁵
F3	1.06± 1.13	1.23± 0.02	0.0487±0.0079	0.311±0.027	1.397±0.270	0.00/0.00	–	–	2.6 10 ⁻¹ /1.5 10 ⁻²
F4	2.08± 0.25	1.13± 0.02	0.0508±0.0043	0.350±0.016	1.674±0.142	0.00/0.00	5.5	-4.9/1.00	1.9 10 ⁻³ /8.5 10 ⁻⁶
F5	2.17± 0.31	1.25± 0.05	0.0466±0.0061	0.281±0.035	1.955±0.244	0.00/0.00	–	–	1.1 10 ⁻⁶ /4.0 10 ⁻³
F6	2.29± 0.13	1.25± 0.02	0.0456±0.0017	0.277±0.007	1.690±0.090	0.00/0.00	–	–	4.1 10 ⁻¹ /8.2 10 ⁻¹
F7	2.67± 0.02	1.18± 0.00	0.0477±0.0004	0.310±0.001	1.848±0.013	0.00/0.00	3.5	-7.2/1.00	2.7 10 ⁻¹ /2.2 10 ⁰
G1	2.94± 1.33	1.18± 0.03	0.0488±0.0057	0.312	0.688	0.00/0.00	–	–	4.0 10 ⁻⁷ / –
G2a	1.39± 0.84	1.22± 0.02	0.0503±0.0088	0.313	0.514±0.073	0.00/0.00	–	–	2.3 10 ⁻¹ /1.5 10 ⁻³
G2b	1.21± 0.59	1.22± 0.02	0.0494±0.0186	0.312	0.515±0.050	0.00/0.00	5.5	-5.2/1.00	1.4 10 ⁻¹ /4.3 10 ⁻⁴
G2c	2.51± 0.99	1.19± 0.02	0.0499±0.0051	0.313	0.608±0.093	0.00/0.00	5.5	-3.7/1.00	2.0 10 ⁻¹ /1.7 10 ⁻³
G3	1.12± 1.15	1.22± 0.00	0.0502±0.0239	0.313±0.035	0.493±0.115	0.00/0.00	–	–	2.6 10 ⁻¹ /2.0 10 ⁻²
G4	2.09± 0.25	1.13± 0.02	0.0508±0.0056	0.348±0.021	0.581±0.028	0.00/0.00	3.8	-8.5/1.00	7.5 10 ⁻³ /6.4 10 ⁻¹
G5	2.17± 0.31	1.25± 0.04	0.0471±0.0059	0.281±0.033	0.667±0.082	0.00/0.00	–	–	3.9 10 ⁻⁷ /4.2 10 ⁻³
G6	2.33± 0.12	1.26± 0.02	0.0477±0.0023	0.274±0.010	0.597±0.019	0.00/0.00	–	–	3.6 10 ⁻¹ /8.0 10 ⁻¹
G7	2.16± 0.02	1.27± 0.00	0.0474±0.0007	0.271±0.001	0.586±0.004	0.00/0.00	4.0	-5.7/1.00	4.2 10 ⁻¹ /1.7 10 ⁰
H1	2.90± 1.77	1.18± 0.04	0.0483±0.0063	0.311	0.688	0.00/0.00	–	–	7.4 10 ⁻⁸ / –
H2a	1.63± 0.86	1.21± 0.02	0.0494±0.0055	0.312	0.534±0.087	0.00/0.00	–	–	2.0 10 ⁻¹ /4.7 10 ⁻⁴
H2b	1.87± 0.78	1.20± 0.02	0.0491±0.0052	0.312	0.563±0.096	0.00/0.00	5.5	-4.5/1.00	1.2 10 ⁻¹ /5.0 10 ⁻⁴
H2c	2.12± 0.98	1.20± 0.02	0.0493±0.0052	0.312	0.582±0.087	0.00/0.00	5.5	-4.1/1.00	2.2 10 ⁻¹ /9.4 10 ⁻⁴
H3	1.80± 1.14	1.23± 0.01	0.0490±0.0053	0.301±0.020	0.550±0.097	0.00/0.00	–	–	2.6 10 ⁻¹ /1.7 10 ⁻²
H4	2.09± 0.25	1.13± 0.02	0.0509±0.0045	0.349±0.016	0.581±0.040	0.00/0.00	5.5	-4.7/1.00	1.5 10 ⁻³ /1.6 10 ⁻⁶
H5	2.17± 0.34	1.25± 0.06	0.0467±0.0066	0.280±0.048	0.671±0.110	0.00/0.00	–	–	1.4 10 ⁻⁶ /4.0 10 ⁻³
H6	2.29± 0.12	1.27± 0.02	0.0481±0.0023	0.273±0.010	0.605±0.021	0.00/0.00	–	–	4.1 10 ⁻¹ /8.1 10 ⁻¹
H7	2.19± 0.02	1.27± 0.00	0.0486±0.0007	0.273±0.001	0.598±0.004	0.00/0.00	4.3	-5.0/1.00	4.6 10 ⁻¹ /1.7 10 ⁰
II	2.95± 1.23	1.18± 0.03	0.0485±0.0053	0.311	0.688	0.15/0.00	–	–	3.2 10 ⁻¹² / –

Table A.4. continued.

Model	Age (Gyr)	M/M_{\odot}	$(Z/X)_0$	Y_0	α_{mlt}	$\alpha_{\text{ov}} / \xi_{\text{PC}}$	b_{SE}	$a_{\text{SE}}/r_{\text{SE}}$	$\chi^2_{\text{R,classic}} / \chi^2_{\text{R,seism}}$
I2a	2.49± 0.85	1.19± 0.02	0.0494±0.0051	0.312	0.602±0.096	0.15/0.00	–	–	1.3 10 ⁻¹ /5.7 10 ⁻⁴
I2b	1.85± 0.77	1.20± 0.02	0.0492±0.0055	0.312	0.560±0.094	0.15/0.00	5.5	-4.5/1.00	1.3 10 ⁻¹ /4.8 10 ⁻⁴
I2c	2.07± 0.97	1.20± 0.02	0.0494±0.0058	0.312	0.576±0.084	0.15/0.00	5.5	-4.2/1.00	2.4 10 ⁻¹ /9.9 10 ⁻⁴
I3	1.99± 1.33	1.23± 0.03	0.0490±0.0053	0.299±0.023	0.564±0.092	0.15/0.00	–	–	2.6 10 ⁻¹ /1.5 10 ⁻²
I4	2.08± 0.24	1.18± 0.02	0.0497±0.0049	0.320±0.016	0.577±0.038	0.15/0.00	5.5	-4.3/1.00	8.0 10 ⁻² /9.3 10 ⁻⁴
I5	2.03± 0.37	1.39± 0.02	0.0425±0.0047	0.204±0.004	0.703±0.121	0.15/0.00	–	–	2.2 10 ⁻¹ /8.5 10 ⁻¹
I6	2.22± 0.11	1.20± 0.01	0.0482±0.0024	0.303±0.006	0.591±0.029	0.15/0.00	–	–	2.9 10 ⁻¹ /4.5 10 ⁰
I7	2.17± 0.02	1.27± 0.00	0.0488±0.0007	0.274±0.001	0.596±0.004	0.15/0.00	4.4	-4.8/1.00	4.7 10 ⁻¹ /3.0 10 ⁰
J1	3.02± 1.39	1.18± 0.03	0.0487±0.0056	0.311	0.688	1.80/0.00	–	–	7.0 10 ⁻⁶ / –
J2a	1.66± 0.85	1.21± 0.02	0.0497±0.0066	0.313	0.532±0.082	1.80/0.00	–	–	2.1 10 ⁻¹ /5.8 10 ⁻⁴
J2b	1.73± 0.74	1.21± 0.02	0.0492±0.0061	0.312	0.548±0.089	1.80/0.00	5.5	-4.8/1.00	1.4 10 ⁻¹ /4.1 10 ⁻⁴
J2c	2.06± 0.91	1.20± 0.02	0.0495±0.0070	0.312	0.571±0.078	1.80/0.00	5.5	-4.4/1.00	2.5 10 ⁻¹ /4.7 10 ⁻⁴
J3	1.99± 0.95	1.23± 0.01	0.0493±0.0057	0.301±0.019	0.560±0.099	1.80/0.00	–	–	2.6 10 ⁻¹ /1.4 10 ⁻²
J4	2.02± 0.22	1.13± 0.02	0.0517±0.0048	0.356±0.015	0.569±0.041	1.80/0.00	5.5	-5.1/1.00	5.5 10 ⁻⁷ /1.2 10 ⁻⁵
J5	0.80± 0.24	1.43± 0.07	0.0442±0.0052	0.200±0.048	0.890±0.282	1.80/0.00	–	–	5.3 10 ⁻¹ /6.8 10 ⁰
J6	1.73± 0.09	1.21± 0.02	0.0528±0.0022	0.315±0.008	0.585±0.020	1.80/0.00	–	–	2.4 10 ⁻¹ /8.3 10 ⁰
J7	2.02± 0.01	1.23± 0.00	0.0489±0.0008	0.296±0.001	0.566±0.003	1.80/0.00	4.2	-6.5/1.00	3.1 10 ⁻¹ /5.5 10 ⁰
K1	2.87± 1.22	1.17± 0.03	0.0448±0.0049	0.307	0.688	0.00/1.30	–	–	1.2 10 ⁻⁵ / –
K2a	2.43± 0.86	1.18± 0.02	0.0452±0.0049	0.307	0.600±0.095	0.00/1.30	–	–	1.5 10 ⁻¹ /1.1 10 ⁻³
K2b	1.70± 0.74	1.20± 0.02	0.0450±0.0052	0.307	0.547±0.093	0.00/1.30	5.5	-4.7/1.00	1.3 10 ⁻¹ /4.8 10 ⁻⁴
K2c	2.32± 0.96	1.19± 0.02	0.0450±0.0049	0.307	0.592±0.090	0.00/1.30	5.0	-4.7/1.00	2.4 10 ⁻¹ /5.4 10 ⁻⁴
K3	2.11± 1.06	1.22± 0.02	0.0450±0.0049	0.293±0.019	0.575±0.109	0.00/1.30	–	–	2.7 10 ⁻¹ /1.2 10 ⁻²
K4	2.12± 0.24	1.12± 0.02	0.0464±0.0044	0.347±0.016	0.577±0.044	0.00/1.30	5.5	-4.7/1.00	1.3 10 ⁻³ /1.6 10 ⁻⁶
K5	2.18± 0.31	1.25± 0.03	0.0438±0.0050	0.275±0.023	0.682±0.075	0.00/1.30	–	–	3.2 10 ⁻⁶ /1.6 10 ⁻³
K6	1.92± 0.07	1.24± 0.01	0.0489±0.0014	0.292±0.003	0.603±0.012	0.00/1.30	–	–	1.4 10 ⁰ /8.9 10 ⁻¹
K7	2.14± 0.01	1.22± 0.00	0.0494±0.0006	0.301±0.001	0.592±0.003	0.00/1.30	3.8	-6.5/1.00	6.1 10 ⁻¹ /2.7 10 ⁰

Table A.5. Same as Table 5 but for different input physics of the models (see Sect. 3 and Tables 2 and 3).

Model	T_{eff} [K]	L [L_{\odot}]	[Fe/H] [dex]	$\log g$ [dex]	R [R_{\odot}]	$\langle \Delta \nu \rangle$ [μHz]	ν_{max} [μHz]	$\langle r_{02} \rangle$ —	$\langle rr_{01/10} \rangle$ —	X_C —	$\frac{\Delta Y}{\Delta Z}$ —	R_{cc} [R_{\star}]	R_{zc} [R_{\star}]	$M_{\text{p}} \sin i$ [M_{Jupiter}]
B1	6116.	2.053	0.22	4.30	1.28	101.45	2138.	0.078	0.034	0.31	2.0	0.027	0.779	1.18±0.03
B2a	6038.	2.064	0.22	4.28	1.32	98.13	2072.	0.088	0.035	0.40	2.0	0.020	0.821	1.19±0.03
B2b	6053.	2.063	0.22	4.28	1.31	98.13	2073.	0.084	0.034	0.36	2.0	0.023	0.806	1.18±0.03
B2c	6053.	2.063	0.22	4.28	1.31	98.21	2073.	0.084	0.034	0.36	2.0	0.023	0.806	1.18±0.03
B3	6022.	2.066	0.22	4.28	1.32	98.14	2087.	0.087	0.034	0.40	1.6	0.017	0.815	1.20±0.03
B4	6116.	2.054	0.22	4.27	1.28	98.14	2028.	0.084	0.035	0.33	3.4	0.034	0.812	1.14±0.03
B5	6116.	2.053	0.22	4.32	1.28	104.12	2250.	0.084	0.033	0.38	1.1	0.011	0.786	1.22±0.05
B6	6016.	2.062	0.21	4.29	1.32	98.28	2109.	0.084	0.034	0.37	1.1	0.013	0.802	1.21±0.03
B7	6012.	2.046	0.23	4.29	1.32	98.28	2099.	0.081	0.034	0.34	1.3	0.019	0.792	1.21±0.03
C1	6116.	2.053	0.22	4.30	1.28	101.39	2139.	0.104	0.034	0.26	2.0	0.011	0.784	1.18±0.04
C2a	6057.	2.062	0.22	4.28	1.31	98.13	2054.	0.074	0.035	0.24	2.0	0.016	0.785	1.17±0.03
C2b	6048.	2.063	0.22	4.29	1.31	98.14	2111.	0.091	0.035	0.43	2.0	0.007	0.837	1.20±0.03
C2c	6048.	2.063	0.22	4.29	1.31	98.20	2112.	0.091	0.035	0.43	2.0	0.007	0.837	1.20±0.03
C3	6021.	2.066	0.22	4.28	1.32	98.14	2088.	0.081	0.034	0.31	1.3	0.004	0.807	1.21±0.04
C4	6108.	2.055	0.22	4.28	1.28	98.13	2046.	0.084	0.036	0.32	3.6	0.018	0.819	1.15±0.03
C5	6117.	2.053	0.22	4.32	1.28	103.73	2244.	0.083	0.033	0.34	1.0	0.000	0.798	1.21±0.04
C6	6024.	2.062	0.23	4.29	1.32	98.45	2119.	0.083	0.034	0.33	1.1	0.003	0.807	1.21±0.03
C7	6013.	2.053	0.22	4.29	1.32	98.27	2118.	0.083	0.034	0.33	1.0	0.001	0.808	1.22±0.03
D1	6116.	2.053	0.22	4.30	1.28	101.73	2143.	0.075	0.032	0.32	2.0	0.043	0.769	1.18±0.03
D2a	6051.	2.063	0.22	4.28	1.31	98.13	2060.	0.077	0.032	0.33	2.0	0.044	0.782	1.18±0.03
D2b	6050.	2.068	0.22	4.29	1.31	98.14	2093.	0.089	0.034	0.43	2.0	0.036	0.818	1.19±0.03
D2c	6049.	2.065	0.22	4.28	1.31	98.20	2080.	0.084	0.034	0.39	2.0	0.040	0.804	1.19±0.03
D3	6022.	2.066	0.22	4.28	1.32	98.14	2087.	0.086	0.034	0.41	1.6	0.034	0.808	1.20±0.04
D4	6103.	2.056	0.22	4.28	1.29	98.13	2039.	0.084	0.033	0.36	3.2	0.049	0.808	1.15±0.03
D5	6115.	2.053	0.22	4.29	1.28	100.74	2128.	0.084	0.033	0.38	2.4	0.040	0.798	1.17±0.05
D6	6020.	2.058	0.19	4.29	1.32	98.31	2100.	0.083	0.034	0.39	1.3	0.030	0.800	1.21±0.03
D7	6047.	2.091	0.22	4.29	1.32	98.30	2102.	0.085	0.033	0.41	1.5	0.036	0.803	1.21±0.03
E1	6103.	2.051	0.22	4.27	1.28	99.04	2030.	0.063	0.040	0.00	2.0	0.032	0.756	1.14±0.05
E2a	6036.	2.064	0.22	4.28	1.32	98.13	2073.	0.095	0.035	0.46	2.0	0.007	0.861	1.19±0.03
E2b	6062.	2.061	0.22	4.29	1.30	98.14	2114.	0.096	0.035	0.48	2.0	0.008	0.859	1.19±0.03
E2c	6069.	2.062	0.22	4.29	1.30	98.20	2091.	0.089	0.035	0.38	2.0	0.005	0.839	1.18±0.03
E3	6023.	2.065	0.22	4.28	1.32	98.14	2086.	0.092	0.035	0.44	1.5	0.004	0.850	1.20±0.04
E4	6044.	2.063	0.23	4.29	1.31	98.17	2108.	0.090	0.035	0.41	1.5	0.004	0.838	1.20±0.03
E5	6116.	2.053	0.22	4.32	1.28	103.98	2251.	0.083	0.033	0.34	0.7	0.000	0.799	1.22±0.04
E6	6107.	2.098	0.28	4.29	1.30	99.19	2096.	0.082	0.035	0.32	2.0	0.016	0.810	1.18±0.03
E7	6015.	2.019	0.23	4.29	1.31	98.37	2127.	0.091	0.034	0.43	1.4	0.003	0.839	1.20±0.03
F1	6116.	2.053	0.22	4.29	1.28	101.37	2128.	0.075	0.033	0.29	2.0	0.028	0.771	1.17±0.03
F2a	6069.	2.061	0.22	4.28	1.30	98.13	2043.	0.066	0.033	0.23	2.0	0.039	0.751	1.16±0.03
F2b	6054.	2.063	0.22	4.28	1.31	98.14	2067.	0.081	0.034	0.33	2.0	0.024	0.798	1.18±0.03
F2c	6071.	2.084	0.22	4.27	1.31	98.17	2035.	0.069	0.034	0.24	2.0	0.038	0.759	1.17±0.03
F3	6022.	2.065	0.22	4.28	1.32	98.14	2087.	0.097	0.035	0.51	2.0	0.017	0.852	1.20±0.03
F4	6108.	2.055	0.22	4.27	1.28	98.13	2034.	0.084	0.035	0.33	3.2	0.033	0.811	1.14±0.03
F5	6116.	2.053	0.22	4.32	1.28	104.16	2251.	0.083	0.033	0.38	1.0	0.011	0.786	1.22±0.04
F6	6009.	2.061	0.19	4.29	1.33	98.28	2110.	0.083	0.034	0.37	0.9	0.010	0.802	1.22±0.03
F7	6085.	2.097	0.21	4.28	1.31	98.29	2061.	0.077	0.034	0.30	2.0	0.027	0.786	1.18±0.03
G1	6116.	2.053	0.22	4.29	1.28	101.33	2126.	0.073	0.033	0.28	2.0	0.030	0.767	1.17±0.04
G2a	6029.	2.065	0.22	4.28	1.32	98.14	2080.	0.093	0.035	0.46	2.0	0.019	0.838	1.20±0.03
G2b	6049.	2.064	0.22	4.29	1.31	98.14	2113.	0.095	0.035	0.48	2.0	0.018	0.842	1.20±0.03
G2c	6056.	2.063	0.22	4.28	1.31	98.19	2064.	0.080	0.034	0.32	2.0	0.026	0.792	1.18±0.03
G3	6022.	2.066	0.22	4.28	1.32	98.14	2086.	0.096	0.035	0.49	2.0	0.019	0.849	1.20±0.03
G4	6114.	2.055	0.21	4.28	1.28	98.30	2046.	0.084	0.035	0.34	3.2	0.033	0.811	1.14±0.03
G5	6116.	2.054	0.22	4.32	1.28	104.10	2251.	0.083	0.033	0.38	1.0	0.012	0.787	1.22±0.04
G6	6010.	2.073	0.21	4.29	1.33	98.29	2122.	0.083	0.034	0.37	0.8	0.012	0.798	1.23±0.03
G7	6007.	2.080	0.21	4.29	1.33	98.28	2128.	0.085	0.034	0.39	0.7	0.011	0.804	1.23±0.03
H1	6116.	2.054	0.22	4.29	1.28	101.32	2126.	0.074	0.033	0.28	2.0	0.030	0.769	1.17±0.04
H2a	6035.	2.065	0.22	4.28	1.32	98.13	2075.	0.090	0.035	0.43	2.0	0.019	0.828	1.19±0.03
H2b	6053.	2.062	0.22	4.28	1.31	98.14	2087.	0.087	0.034	0.39	2.0	0.020	0.817	1.19±0.03
H2c	6054.	2.064	0.22	4.28	1.31	98.20	2077.	0.084	0.034	0.36	2.0	0.022	0.807	1.18±0.03
H3	6022.	2.066	0.22	4.28	1.32	98.14	2086.	0.089	0.034	0.41	1.6	0.017	0.820	1.20±0.03
H4	6109.	2.054	0.22	4.28	1.28	98.13	2036.	0.084	0.035	0.33	3.2	0.032	0.810	1.14±0.03
H5	6116.	2.053	0.22	4.32	1.28	104.17	2253.	0.083	0.033	0.38	1.0	0.011	0.786	1.22±0.05
H6	6014.	2.086	0.22	4.29	1.33	98.38	2125.	0.083	0.034	0.38	0.8	0.013	0.797	1.23±0.03
H7	6011.	2.089	0.23	4.29	1.34	98.29	2125.	0.084	0.034	0.39	0.8	0.013	0.800	1.23±0.03
I1	6116.	2.053	0.22	4.29	1.28	101.29	2127.	0.072	0.021	0.38	2.0	0.088	0.769	1.17±0.03
I2a	6050.	2.063	0.22	4.28	1.31	98.13	2061.	0.078	0.024	0.42	2.0	0.086	0.796	1.18±0.03

Table A.5. continued.

Model	T_{eff} [K]	L [L_{\odot}]	[Fe/H] [dex]	$\log g$ [dex]	R [R_{\odot}]	$\langle \Delta \nu \rangle$ [μHz]	ν_{max} [μHz]	$\langle r_{02} \rangle$ —	$\langle rr_{01/10} \rangle$ —	X_C —	$\frac{\Delta \nu}{\Delta Z}$ —	M_{cc} [M_{\star}]	R_{zc} [R_{\star}]	$M_{\text{p}} \sin i$ [M_{Jupiter}]
I2b	6051.	2.063	0.22	4.28	1.31	98.14	2089.	0.087	0.027	0.48	2.0	0.082	0.818	1.19±0.03
I2c	6053.	2.064	0.22	4.28	1.31	98.19	2080.	0.084	0.026	0.46	2.0	0.083	0.810	1.19±0.03
I3	6022.	2.066	0.22	4.28	1.32	98.14	2087.	0.085	0.027	0.48	1.6	0.078	0.813	1.20±0.04
I4	6065.	2.062	0.22	4.28	1.30	98.14	2072.	0.083	0.026	0.45	2.3	0.086	0.810	1.18±0.03
I5	6044.	2.066	0.20	4.34	1.31	106.11	2392.	0.086	0.031	0.49	0.0	0.000	0.775	1.31±0.04
I6	6041.	2.020	0.22	4.29	1.30	99.37	2119.	0.082	0.026	0.46	1.7	0.078	0.801	1.19±0.03
I7	6011.	2.090	0.23	4.29	1.34	98.30	2126.	0.083	0.027	0.49	0.8	0.071	0.801	1.23±0.03
J1	6116.	2.053	0.22	4.30	1.28	101.35	2130.	0.071	0.012	0.42	2.0	0.125	0.769	1.17±0.04
J2a	6031.	2.065	0.22	4.28	1.32	98.13	2078.	0.090	0.024	0.52	2.0	0.121	0.829	1.20±0.03
J2b	6048.	2.061	0.22	4.29	1.31	98.14	2097.	0.089	0.023	0.51	2.0	0.121	0.824	1.19±0.03
J2c	6051.	2.063	0.22	4.28	1.31	98.19	2085.	0.085	0.021	0.49	2.0	0.122	0.812	1.19±0.03
J3	6022.	2.066	0.22	4.28	1.32	98.14	2087.	0.086	0.022	0.51	1.6	0.119	0.815	1.20±0.03
J4	6116.	2.053	0.22	4.28	1.28	98.13	2037.	0.084	0.020	0.44	3.4	0.134	0.817	1.14±0.03
J5	6228.	2.022	0.24	4.42	1.22	120.50	2807.	0.097	0.031	0.70	0.0	0.085	0.760	1.34±0.05
J6	6081.	2.057	0.26	4.30	1.29	100.14	2149.	0.089	0.023	0.51	2.0	0.122	0.813	1.20±0.03
J7	6014.	2.039	0.22	4.29	1.32	98.28	2113.	0.086	0.022	0.51	1.5	0.116	0.811	1.21±0.03
K1	6116.	2.054	0.22	4.29	1.28	101.54	2124.	0.076	0.034	0.29	2.0	0.021	0.687	1.17±0.04
K2a	6046.	2.063	0.22	4.28	1.31	98.13	2064.	0.086	0.034	0.37	2.0	0.015	0.746	1.18±0.03
K2b	6051.	2.064	0.22	4.28	1.31	98.14	2085.	0.090	0.035	0.42	2.0	0.014	0.762	1.19±0.03
K2c	6055.	2.062	0.22	4.28	1.31	98.20	2063.	0.082	0.034	0.34	2.0	0.018	0.740	1.18±0.03
K3	6022.	2.066	0.22	4.28	1.32	98.14	2087.	0.086	0.034	0.39	1.4	0.011	0.744	1.20±0.03
K4	6109.	2.054	0.22	4.27	1.28	98.13	2025.	0.084	0.035	0.33	3.4	0.027	0.745	1.14±0.03
K5	6116.	2.053	0.22	4.32	1.28	104.40	2247.	0.083	0.033	0.38	1.0	0.007	0.700	1.22±0.04
K6	6061.	2.121	0.26	4.29	1.32	98.46	2111.	0.086	0.034	0.40	1.4	0.018	0.745	1.22±0.03
K7	6011.	2.033	0.26	4.28	1.32	98.31	2089.	0.084	0.034	0.37	1.6	0.017	0.727	1.20±0.03